

CytoNet: A Foundation Model for the Human Cerebral Cortex at Cellular Resolution

Christian Schiffer^{1,2}, Zeynep Boztoprak^{1,2}, Jan-Oliver Kropp^{1,2,3}, Julia Thönnißen¹,
Katia Berr⁴, Hannah Spitzer^{4,5}, Katrin Amunts^{1,3}, and Timo Dickscheid^{1,2,6}

¹Institute of Neuroscience and Medicine (INM-1), Research Centre Jülich, Jülich, Germany

²Helmholtz AI, Research Centre Jülich, Jülich, Germany

³Cécile & Oscar Vogt Institute for Brain Research, University Hospital Düsseldorf, Düsseldorf, Germany

⁴Institute of Computational Biology, Computational Health Center, Helmholtz Munich, Munich, Germany

⁵Institute for Stroke and Dementia Research (ISD), LMU University Hospital, LMU Munich, Germany

⁶Computer Vision, Institute for Computational Visualistics, University of Koblenz, Koblenz, Germany

Abstract

Studying the cellular architecture of the human cerebral cortex is critical for understanding brain organization and function. It requires investigating complex texture patterns in histological images, yet automatic methods that scale across whole brains are still lacking. Here we introduce CytoNet, a foundation model trained on 1 million unlabeled microscopic image patches from over 4,000 histological sections spanning ten postmortem human brains. Using co-localization in the cortical sheet for self-supervision, CytoNet encodes complex cellular patterns into expressive and anatomically meaningful feature representations. CytoNet supports multiple downstream applications, including area classification, laminar segmentation, quantification of microarchitectural variation, and data-driven mapping of previously uncharted areas. In addition, CytoNet captures microarchitectural signatures of macroscale functional organization, enabling decoding of functional network parcellations from cytoarchitectonic features. Together, these results establish CytoNet as a unified framework for scalable analysis of cortical microarchitecture and for linking cellular architecture to structure–function organization in the human cerebral cortex.

1 Introduction

The cerebral cortex of the human brain is divided into cortical areas, each with different functions. Brain areas exhibit complex relationships and hierarchies and are structurally and functionally interconnected. This forms the basis for a wide range of functions underlying cognition and consciousness. Modern neuroscience has addressed the organization of the cerebral cortex in the living human brain with multimodal imaging (Glasser et al., 2016; Mathis et al., 2024). Three-dimensional reconstruction is key to capture complementary organizational principles across scales. For example, the *BigBrain* project (Amunts et al., 2013) has processed

7404 full-brain histological sections to generate a volumetric 3D reconstruction at 20 μm resolution at close-to-the cellular level. Cytoarchitecture is defined by a regionally specific spatial organization of cells into distinct layers, columns, and areas, providing a mechanistic bridge linking multimodal measurements to anatomically well-defined structural entities (Campbell, 1904; Hilgetag et al., 2019; Amunts et al., 2022). This cytoarchitectonic framework has guided cortical mapping for more than a century, from early area maps (Brodmann, 1909; Vogt et al., 1919; Von Economo, 1925) to modern brain atlases (Zilles et al., 2010; Amunts et al., 2015; Ding et al., 2016; Amunts et al., 2020; Casamitjana et al., 2025). Advances in high-throughput microscopy have enabled whole-brain histological imaging and reconstruction at micrometer resolution, producing terabyte-scale datasets comprising thousands of sections from multiple human brains (Amunts et al., 2020). While acquiring such massive and detailed datasets is essential for decoding brain structure and function (Amunts et al., 2024), their analysis demands scalable computational methods (Amunts et al., 2021).

Recent advances in artificial intelligence (AI) suggest a route to address this challenge through large-scale foundation models that learn general-purpose representations from data (Bommasani et al., 2022). Such models have enabled breakthroughs ranging from protein structure prediction (Jumper et al., 2021) to vision (Radford et al., 2021; Oquab et al., 2024) and language (Chowdhery et al., 2023; OpenAI et al., 2024). A key driver of these successes is self-supervised learning, which extracts expressive features from massive unannotated datasets by generating implicit training signals from the data itself (Chen et al., 2020; He et al., 2020). In this novel paradigm, computational approaches shift from designing specialized analysis pipelines to learning general feature representations that directly support data-driven investigation, prediction, and discovery in large-scale datasets. In neuroimaging, analogous approaches are emerging to learn transferable representations that enable adaptation to diverse downstream prediction tasks, for example from MRI (Tak et al., 2026) and fMRI (Dong et al., 2024) datasets. At the cellular scale, histological data provides direct access to cortical microarchitecture, motivating foundation models that learn transferable cytoarchitectonic representations from whole-brain microscopy and relate them to macroscale cortical organization and functional systems.

To this end, we introduce CytoNet, a foundation model for human cortical organization, trained with self-supervised learning on 1 million microscopic image patches from over 4,000 cell-body-stained histological sections spanning ten postmortem human brains. CytoNet provides a data-driven approach to quantifying cortical cytoarchitecture by embedding local histological patterns into a continuous feature space that transfers across brains and downstream tasks. Trained using the proposed SpatialNCE loss, a contrastive learning objective that leverages spatial co-localization within the cortical sheet as a self-supervised training signal, CytoNet learns to encode image patches into expressive representations of cytoarchitecture, without requiring manual annotations. We show that these representations are anatomically meaningful and robust. They generalize across brains and spatial scales, while capturing both common cytoarchitectonic structure and brain-specific variation that facilitate cross-brain comparison at whole-brain scale. This shared representation enables cytoarchitectonic mapping, prediction, and exploration at scale, beyond what is practical with task-specific approaches. In cytoarchitectonic area mapping, CytoNet enables accurate classification of over 100 cortical areas, outperforming training from scratch, general self-supervised baselines (Chen et al., 2020), and specialized approaches (Schiffer et al., 2021a). CytoNet also supports label-efficient cortical layer segmentation, producing reliable laminar maps with only a handful of annotated training samples. Beyond mapping, CytoNet features accurately model structural variables, including layer-wise cell densities, outperforming established profile-based descriptors (Wagstyl et al., 2022). If cytoar-

chitecture provides a substrate for systems-level specialization (Mesulam, 1998; Hilgetag et al., 2016), microarchitectural representations should carry information about macroscale functional organization. We therefore test whether CytoNet features can decode widely used functional network parcellations, using spatially aware validation to control for spatial smoothness. Finally, we provide a proof-of-concept that CytoNet features can drive unsupervised mapping of previously unknown regional structures. Together, these results establish CytoNet as a scalable framework for learning, quantifying, and comparing cortical cytoarchitecture from whole-brain histology, enabling systematic analyses across thousands of sections and entire human brains.

2 Results

We present the results of CytoNet from three complementary perspectives. First, we introduce a pretraining strategy that allowed the model to learn from large-scale histological data without annotations. Second, we analyze the learned feature space, using dimensionality reduction and clustering metrics to assess how it reflects local, global, and inter-subject cytoarchitectonic variation. Third, we demonstrate its utility in downstream applications, including prediction of structural variations, cortical area and layer segmentation, decoding of functional organization, and unsupervised mapping of uncharted areas. Together, these results demonstrate CytoNet’s scalability and versatility, showing how a single representation supports diverse analyses.

2.1 CytoNet learns cortical cytoarchitecture from spatial proximity

CytoNet encompasses a family of deep neural networks trained in a self-supervised setting to map cortical image patches to high-dimensional feature vectors that capture cytoarchitectonic properties (Figure 1). Square patches (2,048 px at 2 $\mu\text{m}/\text{px}$, covering 4 mm^2) were sampled along the cortex from ten postmortem brains, with nine used for pretraining and one held out for transfer evaluation.

To train CytoNet, we introduced SpatialNCE, a contrastive objective that encourages patches from nearby cortical locations to map to similar representations. This leverages the anatomical continuity of the cortex as a heuristic for defining similarity, enabling scalable training on large unlabeled datasets without augmentations or manual annotations. SpatialNCE builds on InfoNCE (Oord et al., 2019), the basis of many modern contrastive methods (Caron et al., 2020; Chen et al., 2020; He et al., 2020; Zbontar et al., 2021; Bardes et al., 2022), but uses distances in a shared coordinate space instead of image augmentations as proxy for semantic similarity.

In natural images, positive pairs are often created by augmentations that preserve semantic similarity while disrupting irrelevant features. For the type of data used for CytoNet, this assumption is problematic: common transformations can alter cytoarchitectonic structure, while confounding features such as blood vessels or folding geometry often remain unchanged (Tian et al., 2020; K ugelgen et al., 2021). Supervised contrastive learning (Khosla et al., 2020; Schiffer et al., 2021a) circumvents this issue by using labels, but is limited by annotation cost.

SpatialNCE overcomes both issues by defining similarity directly from anatomical proximity. Given a batch of image patches x_i with corresponding 3D coordinates p_i and normalized neural network features $z_i = f(x_i)$, the loss for patch i is:

$$\mathcal{L}_i = -\frac{1}{\sum_{j \neq i} \omega_{ij}} \sum_{j \neq i} \omega_{ij} \log \frac{\exp(z_i^\top z_j / \tau)}{\sum_{k \neq i} \exp(z_i^\top z_k / \tau)}, \quad (1)$$

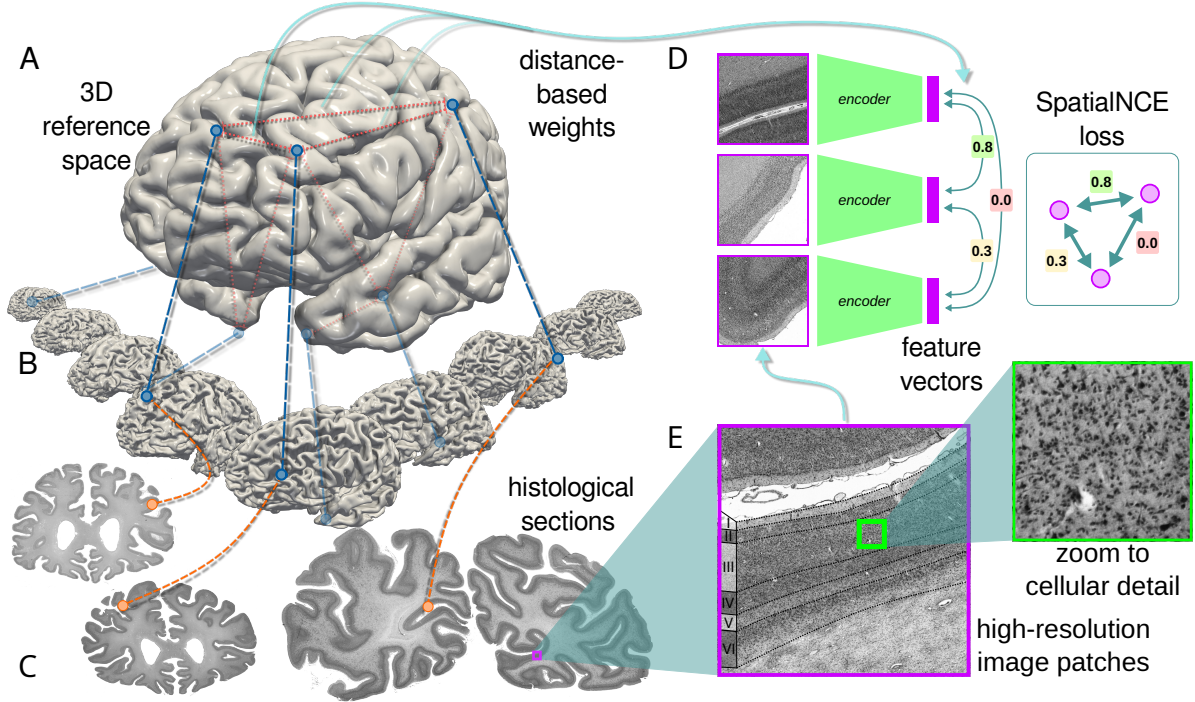


Figure 1: Illustration of the self-supervised pretraining workflow using the proposed SpatialNCE loss in CytoNet. Spatial transformations between the MNI Colin 27 (Holmes et al., 1998) 3D reference coordinate space (A) and microscopic scans of histological brain sections (C) of postmortem human brains (B) were used to link high-resolution microscopic image patches (E) with corresponding 3D locations in the common reference space, allowing to estimate distances between sampled image patches from different brains. These were used to compute similarity scores for the proposed SpatialNCE contrastive loss (D), which promotes extraction of expressive feature vectors for each image patch.

with temperature τ and similarity weights defined by the radial basis function (RBF) kernel

$$\omega_{ij} = \exp\left(-\frac{\|p_i - p_j\|^2}{2\sigma^2}\right) \quad (2)$$

with bandwidth σ . All sections were co-registered to the MNI Colin 27 single subject reference space (Holmes et al., 1998), enabling consistent distance computation across brains. Crucially, the model never receives spatial coordinates, and therefore similarity must be inferred from image content. Unlike augmentation-based methods that impose semantic invariance externally, SpatialNCE exploits the intrinsic continuity of brain organization, encouraging features that capture shared cytoarchitectonic properties (e.g., cell density, lamination) while suppressing confounds (e.g., staining variation or morphology).

The SpatialNCE loss can be used with any neural network architecture. We evaluated ResNet50 (He et al., 2016) and hybrid ResNet50-ViT-B (Dosovitskiy et al., 2020) models with modified input layers to handle large input patches. To process the large datasets in reasonable timeframes (up to 4 TB per epoch, 600 TB per training), models were trained on 16 compute nodes (64 Nvidia A100 40 GB GPUs) of the supercomputer JURECA-DC (Thörnig, 2021) at Jülich Supercomputing Centre, with a runtime of up to 28 hours.

2.2 CytoNet encodes cytoarchitectonic organization

We examined how CytoNet-ViT (1M) organizes cytoarchitectonic information in its feature space (Figure 2, top¹). CytoNet-ViT (1M) is a hybrid ResNet50-ViT-B model pretrained on one million cortical patches. 2D UMAP embeddings (McInnes et al., 2018) of patches from all ten brains revealed distinct brain-specific manifolds (Calinski-Harabasz index (Caliński et al. (1974), CHI) 2517.84) with consistent internal organization: atlas labels indicating different cytoarchitectonic areas (Amunts et al., 2020) clustered coherently (CHI 719.66). The second UMAP dimension showed a subdivision of clusters at the central sulcus, which is an important anatomical landmark separating motor and somatosensory areas. The tenth brain (B09), which was not included in the pretraining phase, appeared more compact than the remaining nine. Yet, it showed comparable internal structure, indicating generalization beyond the training set.

To assess how well CytoNet features express cytoarchitectonic similarity across brains, pairwise cosine similarities of feature vectors were mean-aggregated into similarity matrices grouped by atlas areas (Figure 2, bottom). Resulting matrices exhibited a strong block structure, i.e., there was higher similarity within areas than between them. These patterns were highly correlated across subjects (Pearson $r = 0.88 \pm 0.09$), confirming that CytoNet encodes stable inter-area relationships. The tenth brain again showed elevated overall similarity and weaker block structure, consistent with the reduced specificity observed in the UMAP embeddings.

Further, we studied the attention maps of the class token in the first vision transformer layer to visualize how the model attends to cytoarchitectonic structures. Figure 3 shows attention scores for example patches from the primary visual cortex hOc1 (Brodmann area 17, Amunts et al. (2000)), the (anterior) primary motor cortex area 4a (Geyer et al., 1996) and area 3b of the primary somatosensory cortex (Geyer et al., 1999). The attention scores reveal how the model attends to the composition of cortical layers that define cytoarchitecture. In particular, attention heads focusing on prominent landmarks like the stripe of Gennari in hOc1, Betz giant cells in layer V of 4a, and a pronounced layer V in 3b were identified.

2.3 Applications of CytoNet

The representations learned by CytoNet provide a versatile foundation for multiple downstream applications in human brain mapping. To demonstrate their utility, we evaluated CytoNet features in four complementary settings: (1) correlation with established structural and cytoarchitectonic properties, (2) decoding of macroscale functional organization, (3) supervised mapping tasks such as brain area classification and cortical layer segmentation, and (4) analyses for data-driven mapping of new or refined cortical areas.

Predicting structural variation in cytoarchitecture

We assessed which anatomical properties are reflected in the feature space of CytoNet-ViT (1M), focusing on morphological and cytoarchitectonic variables extracted from B20, the BigBrain dataset (Amunts et al., 2013). The predictive power of CytoNet features was compared to that of intensity profiles extracted from the BigBrain dataset (Wagstyl et al., 2018), which also aim to capture local cytoarchitectonic composition. Intensity profiles mainly reflected anterior-posterior position, whereas CytoNet captured all three spatial axes as well as morphological properties such as cortical thickness, curvature, and cutting angle (Figure 4, A). It also enabled

¹Interactive versions of selected figures are available at <https://go.fzj.de/cytonet-interactive>.

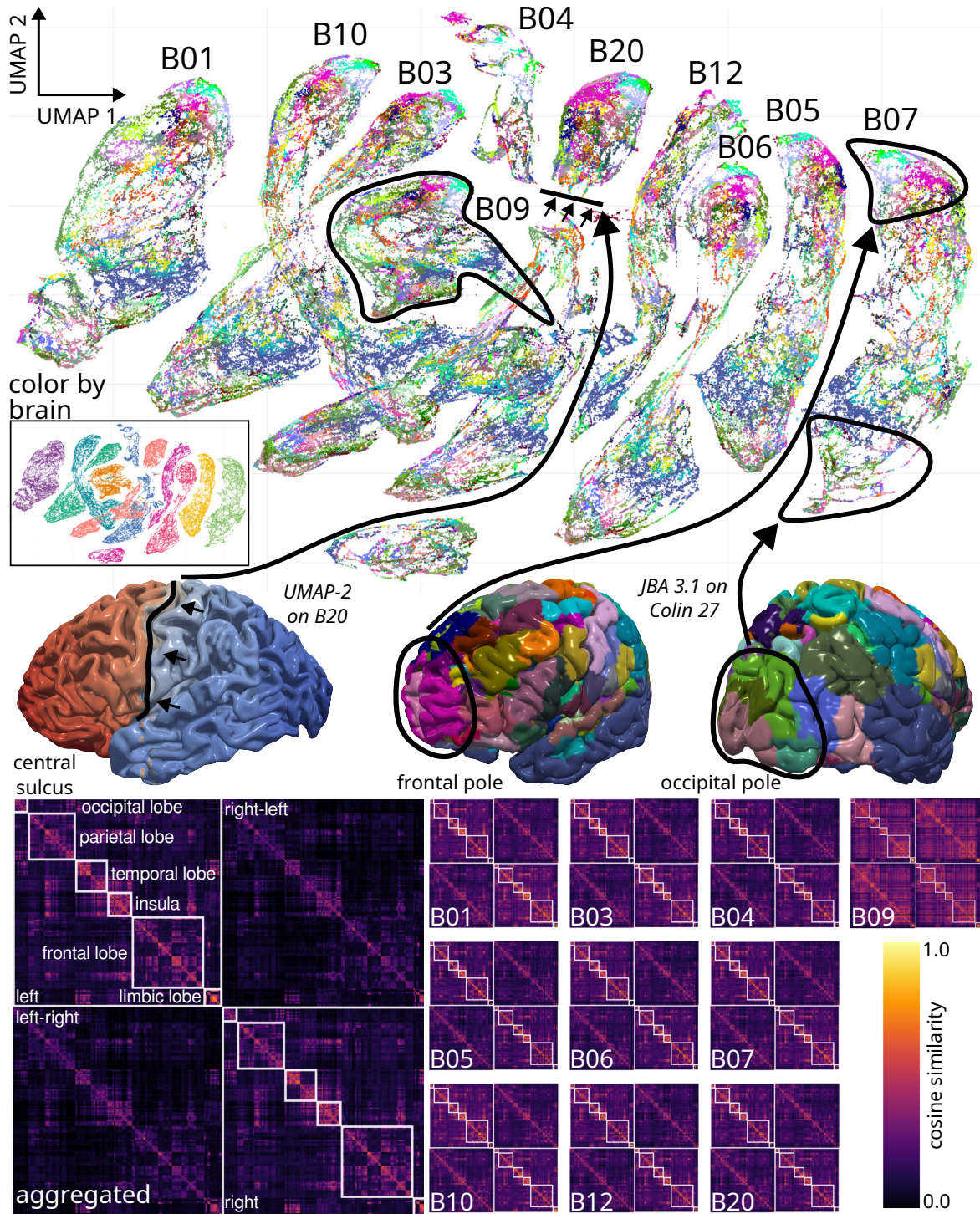


Figure 2: Anatomical plausibility of feature representations learned by CytoNet-ViT (1M). **Top:** 2D UMAP plot of the learned latent space, color coded by maximum probability labels of corresponding coordinates in the Julich Brain atlas (version 3.1, Amunts et al. (2020)), as an approximate assignment to brain areas. Brain-specific clusters fan out along the first UMAP dimension, while the second UMAP dimension shows a transition from the occipital to the frontal pole. A gap along the anterior-posterior axis co-aligns with the central sulcus, marking a prominent structural and functional division. The cluster corresponding to B09 — not included during pretraining — appears more compact than the other clusters, but shows a comparable cytoarchitectonic organization. **Bottom:** Aggregated pairwise cosine similarity of features across ten brains. Cosine similarity was computed between feature vectors from image patches, grouped by Julich Brain Atlas labels and averaged over all area pairs. Rows and columns represent brain areas, ordered by hemisphere, lobe, and label; area names are omitted for clarity (see supplementary Table 3).

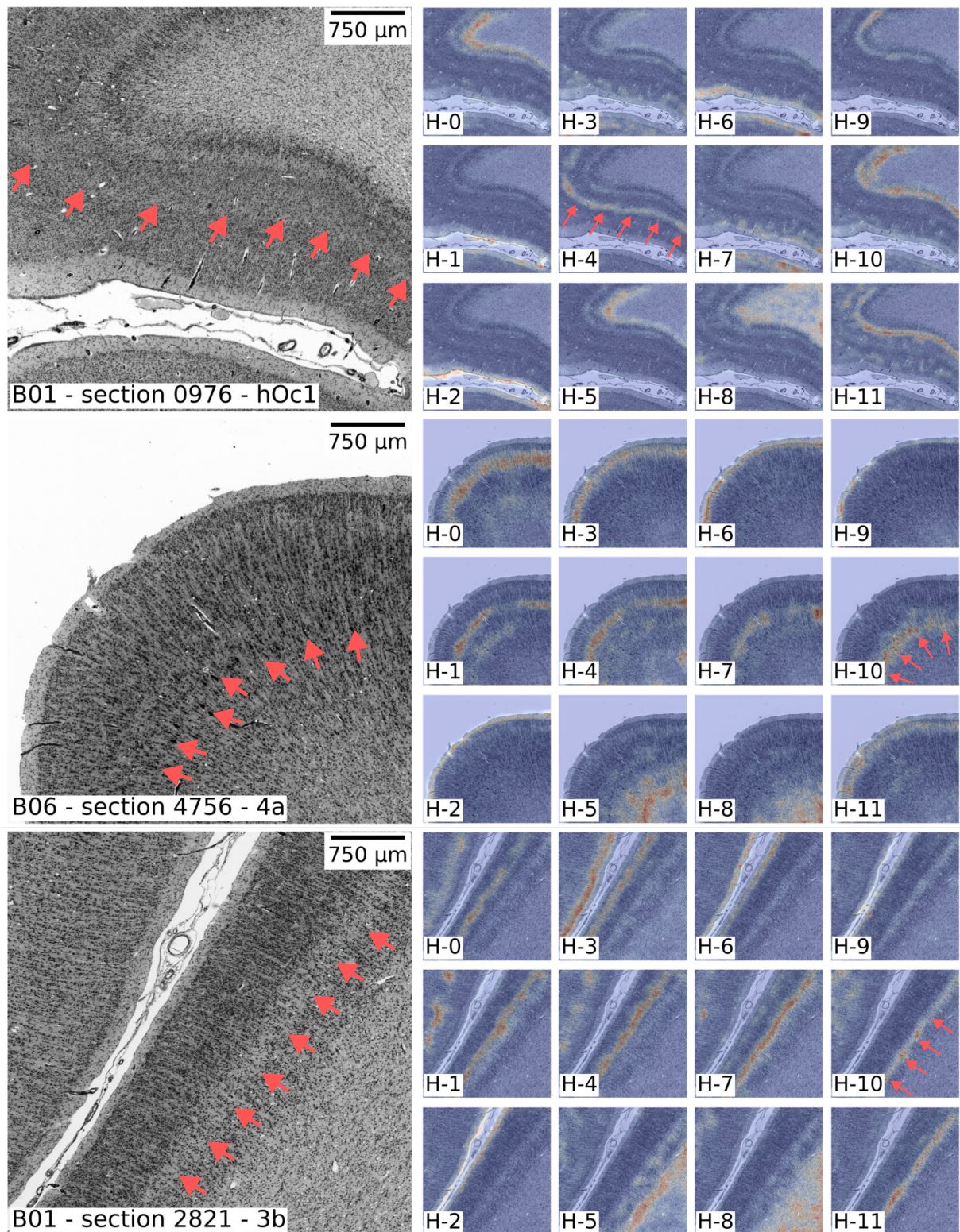


Figure 3: Attention maps from the first self-attention layer of CytoNet-ViT (1M). The figure includes example patches from areas hOc1 (primary visual cortex, Amunts et al. (2000)), 4a (primary motor cortex, Geyer et al. (1996)), and 3b (primary somatosensory cortex, Geyer et al. (1999)). Each row shows the input image (left) and attention scores of all 12 heads overlaid on the image (red = stronger attention). Highlighted are the stripe of Gennari in the primary visual cortex (top), Betz giant cells in layer V of motor cortex (center), and a pronounced layer IV in somatosensory cortex (bottom). Attention scores were gamma transformed ($\gamma = 0.5$) to aid visualization.

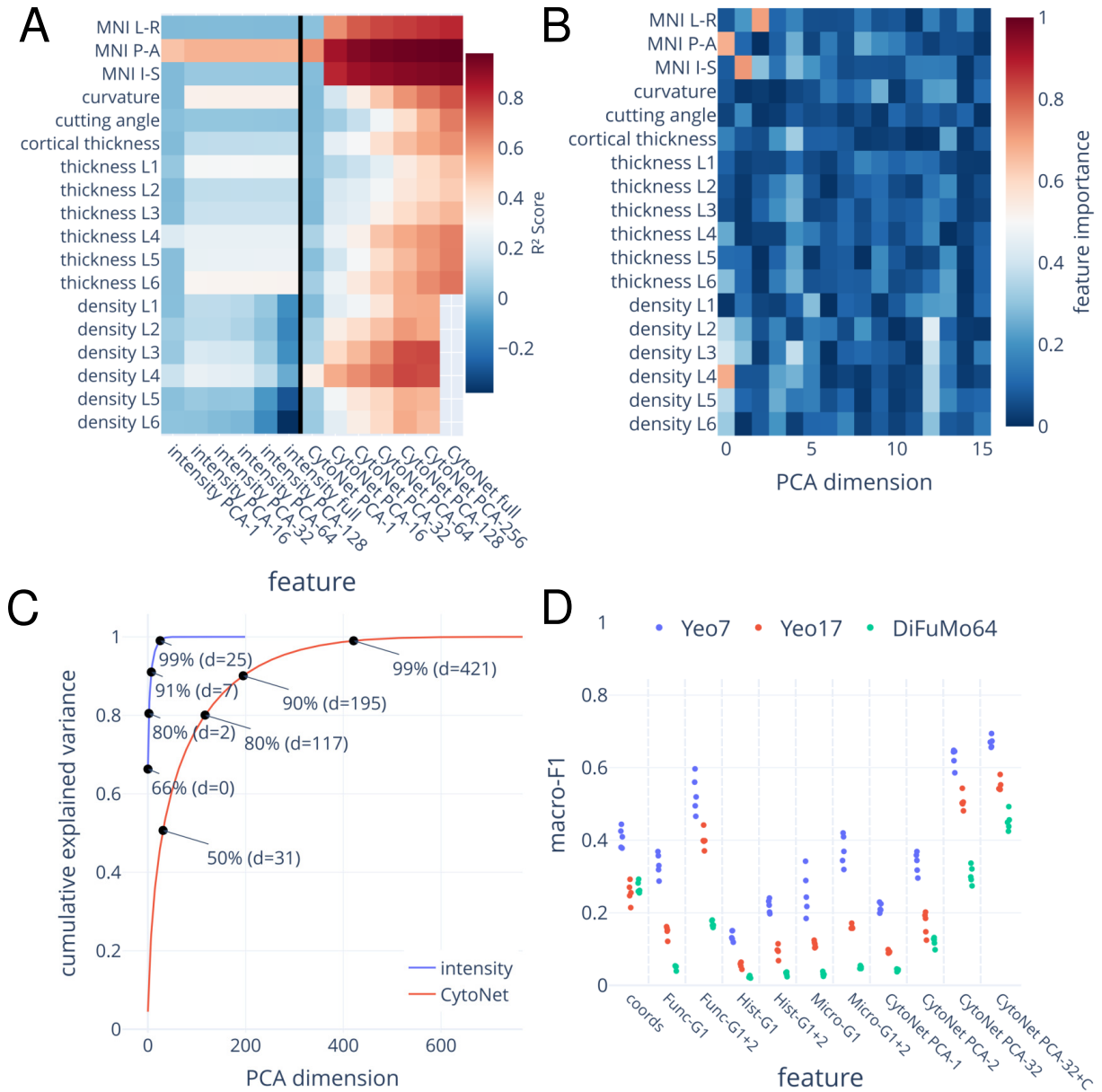


Figure 4: Decoding structural properties and functional parcellations from CytoNet representations in B20. **A:** Linear regression models using varying subsets of PCA components revealed substantially higher R^2 scores for CytoNet features compared to intensity profiles across all evaluated structural and morphological properties. Reported values reflect the R^2 across 5-fold cross-validation. CytoNet PCA- N indicates the first N PCA components of CytoNet features. **B:** Absolute feature importance scores derived from regression coefficients for the first 32 PCA components of CytoNet features showed that components 1–3 were strongly associated with spatial location in MNI space and the density of cortical layer IV, while other properties were predominantly encoded in higher components. LI to L6 denote cortical layers I to VI. **C:** The cumulative explained variance across PCA components indicates that CytoNet features capture substantially more variance than intensity profiles. **D:** Decoding functional parcellation labels (Yeo7, Yeo17; Yeo et al. (2011), and DiFuMo64; Dadi et al. (2020)) from different feature sets using multinomial logistic regression. Reported values reflect macro-F1 across 5-fold cross-validation. CytoNet features outperformed histological (Hist-G, Paquola et al. (2019)) and microstructural (Micro-G, Royer et al. (2022)) gradient baselines as well as a low-dimensional functional-gradient reference (Func-G, Margulies et al. (2016)). A baseline using only fs_LR vertex coordinates quantifies the contribution of cortical location. Concatenating CytoNet features with coordinates (CytoNet PCA-32+C) yields the highest score, indicating complementary information beyond spatial position.

accurate prediction of cortical layer thicknesses and layer-wise cell densities, which intensity profiles from the 20 micrometer model failed to represent consistently (Figure 4, A, left columns). Across all evaluated properties, higher-dimensional PCA projections of CytoNet features generally improved predictive accuracy, while performance of intensity profile projections remained largely constant (Figure 4, B). This indicates that CytoNet encodes a richer set of structural cues that are distributed across many dimensions of the feature space, enabling fine-grained modeling of complex cytoarchitectonic patterns. Consistent with this finding, the cumulative explained variance of the PCA projections was markedly higher for CytoNet features than for intensity profiles, suggesting that CytoNet learns a more structured and informative representation space for downstream analysis (Figure 4, C).

Decoding functional organization from cytoarchitecture

We evaluated whether CytoNet representations can decode macroscale functional organization. To this end, we trained multinomial logistic regression models to predict network labels from the Yeo7 and Yeo17 parcellations (Yeo et al., 2011) as well as the DiFuMo atlas (Dadi et al., 2020) with 64 functional modes, denoted as DiFuMo64 (Figure 4, D).

Cortical location alone provided a strong baseline, consistent with the spatial smoothness of functional networks. Using only fs_LR (32k) vertex coordinates (Van Essen et al., 2012) achieved macro-F1 of 0.40 ± 0.03 (Yeo7), 0.28 ± 0.03 (Yeo17), and 0.25 ± 0.03 (DiFuMo64). CytoNet features provided substantial additional predictive signal, and performance increased systematically with feature dimensionality: PCA-1 reached 0.21 ± 0.02 , 0.10 ± 0.01 , and 0.04 ± 0.01 (Yeo7/Yeo17/DiFuMo64), PCA1-2 reached 0.33 ± 0.04 , 0.18 ± 0.03 , and 0.12 ± 0.01 , and PCA-32 reached 0.63 ± 0.03 , 0.51 ± 0.03 , and 0.31 ± 0.02 . To test whether CytoNet’s advantage over coordinates could be explained by inherent spatial smoothness alone, we performed a spin-based spatial null on the parcellation labels in fs_LR space and assessed the significance of the CytoNet-coordinate macro-F1 delta. The improvement was significant for Yeo17 (10,000 spins; one-sided $p = 0.0036$; Holm-Bonferroni corrected across the three parcellations tested), Yeo7 showed an uncorrected effect ($p = 0.042$); DiFuMo64 was not significant ($p = 0.98$). Notably, while overall decoding was higher for the coarser Yeo7 parcellation, evidence for an improvement beyond spatial smoothness was stronger for the finer-grained Yeo17 labels under the spin null, consistent with CytoNet capturing microarchitectural information beyond coarse spatial gradients.

Compared to gradient baselines, CytoNet PCA-32 outperformed both histological (Hist-G, Paquola et al. (2019)) and microstructural (Micro-G, Royer et al. (2022)) gradients across all targets (Hist-G1+2 0.21 ± 0.02 , 0.09 ± 0.01 , 0.03 ± 0.01 ; Micro-G1+2 0.34 ± 0.04 , 0.17 ± 0.02 , 0.06 ± 0.01). Interestingly, it also exceeded a low-dimensional functional-gradient reference (Func-G1+2: 0.51 ± 0.02 , 0.40 ± 0.03 , 0.17 ± 0.02 ; Margulies et al., 2016), indicating that discrete network assignments can require feature combinations not fully captured by only two functional gradient axes.

Finally, combining CytoNet with explicit spatial information yielded the best performance. Concatenating vertex coordinates with CytoNet PCA-32 increased macro-F1 to 0.67 ± 0.03 (Yeo7), 0.56 ± 0.03 (Yeo17), and 0.44 ± 0.02 (DiFuMo64), suggesting that cytoarchitectonic cues and cortical position provide complementary information for decoding functional parcellations.

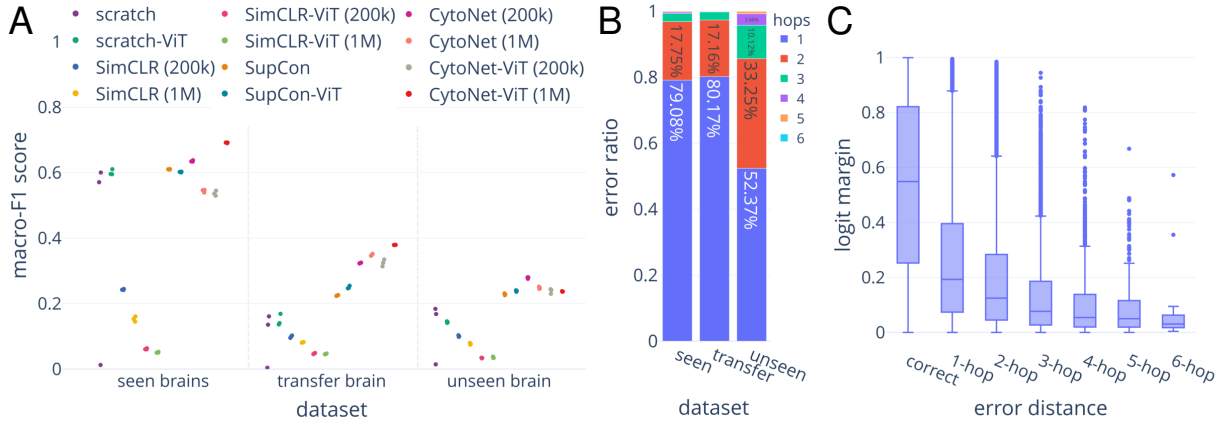


Figure 5: Performance of cytoarchitectonic brain area classification using CytoNet.

A: Macro-F1 scores obtained by linear probing of different models across three training runs. See supplementary Table 5 for more detailed scores. If applicable, the number of pretraining samples are indicated after the model name. **B:** Distribution of prediction errors of CytoNet-ViT (1M) by error distance for seen, transfer, and unseen brains. Error distance was defined as the number of hops between the predicted and true brain area in the adjacency graph of the Julich Brain Atlas 3.1 (Amunts et al., 2020), where 1-hop errors correspond to directly adjacent areas, and larger distances reflect increasing topological separation. **C:** Boxplots of the logit margins for CytoNet-ViT (1M) predictions stratified by error distance. The logit margin—the difference between the top two logits—serves as a proxy for model confidence and distance to the decision boundary (Ngnawé et al., 2024). Correct predictions reveal higher confidence, while incorrect predictions show decreasing confidence with increasing error distance.

Mapping of brain areas and cortical layers

We next evaluated whether CytoNet features support explicit mapping of cytoarchitectonic organization in supervised tasks. Two complementary settings were considered: (i) classification of cytoarchitectonic areas across multiple brains and (ii) segmentation of cortical layers within histological image patches.

In area classification, CytoNet consistently outperformed models trained from scratch, SimCLR (Chen et al., 2020), and supervised contrastive baselines (Schiffer et al., 2021a) across seen, transfer, and unseen brains (Figure 5, A and supplementary Table 5, see Section 4.5 for model details). CytoNet-ViT (1M) reached the best scores on seen brains (macro-F1 0.69 with linear probing, 0.71 with finetuning), surpassing all supervised alternatives and SimCLR. On the transfer brain, where no area annotations were available for training, CytoNet again achieved the highest scores. Even on the unseen brain, which was excluded from both pretraining and classifier training, CytoNet models remained competitive, with compact CNN-based variants showing the strongest generalization. In contrast, SimCLR variants performed poorly across all splits, often below training from scratch. Retrieval analysis confirmed this shortcut learning, showing that SimCLR features clustered images by tissue morphology and vascular patterns rather than area identity (see supplementary Figure 10).

Error analysis (Figure 5, B) revealed that CytoNet’s misclassifications were largely confined to borders between adjacent areas: $\sim 80\%$ of errors in seen and transfer brains occurred within 1 hop of the correct area in the atlas adjacency graph, and over 95% within 2 hops. For the unseen brain, these proportions were somewhat lower (52% and 85%), but errors remained topologically plausible. Confidence, measured by logit margin (Ngnawé et al., 2024), was significantly higher

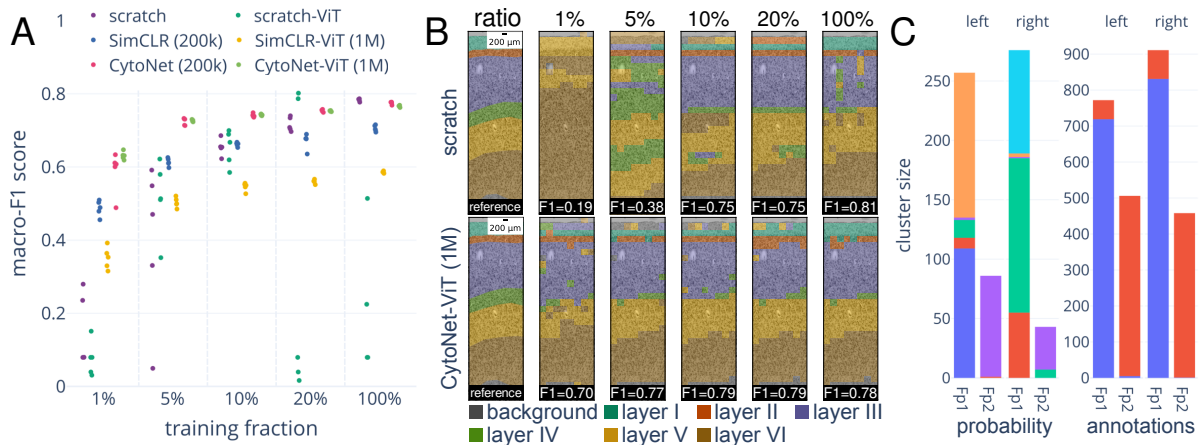


Figure 6: Results for cortical layer segmentation and data-driven mapping of brain areas. **A:** Macro-F1 scores from linear probing of different models with varying amounts of training data across five-fold cross-validation, evaluated on a dedicated test set (also see supplementary Table 7). If applicable, the number of pretraining samples are indicated after the model name. **B:** Example segmentation of cortical layers in area 44 (Amunts et al. (1999)) from the test set for scratch and CytoNet-ViT (1M) models for increasing fractions of the training set. **C:** K-means clusters of CytoNet-ViT (1M) features in the vicinity of frontal pole areas Fp1 and Fp2 in brain B06, with clusters pre-localized using Julich Brain Atlas 3.1 probability maps (threshold 50%) and annotations. Clustering was performed separately based on probabilities (left) and annotations (right). Colors indicate cluster assignment. Results are shown per hemisphere, but clustering was performed jointly across hemispheres.

for correct predictions and decreased systematically with error distance (Figure 5, F). These findings indicate that CytoNet’s errors mirror the uncertainties faced by human experts, with most mistakes arising at difficult borders rather than random misclassifications.

Cortical layer segmentation further demonstrated the richness and data efficiency of CytoNet features. Using only 1% of the annotated dataset (7 training patches), linear probing of CytoNet-ViT (1M) reached a macro-F1 of 0.63, i.e., over four times the scratch baseline (0.15) and well above SimCLR-pretrained models (0.49). With 5% of training data, CytoNet already achieved macro-F1 of 0.74, while baselines required 20% of data to reach similar performance (Figure 6, A, B and supplementary Table 7). Finetuning CytoNet improved accuracy with larger training datasets but caused overfitting in small-data regimes and instability in transformer backbones, whereas linear probing remained robust in both cases.

Data-driven mapping of brain areas

We finally asked whether CytoNet features can support exploratory, data-driven refinement of brain parcellations through clustering. Accurately identifying and delineating brain areas remains a central challenge in brain mapping and analysis, particularly in regions lacking anatomical landmarks. While historical cytoarchitectonic map (e.g., Brodmann (1909)) provide a foundational parcellation, many regions have since been identified based on refined histological evidence, often by subdividing existing areas. As a case study, we examined the frontal pole, which was initially defined as Brodmann area 10, but later subdivided into Fp1 and Fp2 by Bludau et al. (2014). We treated the region as if no subdivision were known and tested whether clustering in CytoNet’s feature space could recover the distinction.

CytoNet features from brain B06 were clustered using k -means, applied either to points pre-localized by probabilistic maps or to points annotated as Fp1/Fp2 (Figure 6, C). In the probabilistic setting, one cluster aligned well with Fp2, while Fp1 points split into multiple clusters with inter-hemispheric differences. This resulted in high purity with respect to anatomical labels (0.97 ± 0.02) and hemisphere (0.91 ± 0.02). In the annotation-based setting, clustering robustly separated Fp1 and Fp2, with mean purity 0.94 ± 0.001 . Here, hemisphere information was more evenly distributed across clusters (purity 0.52 ± 0.001), indicating that areal identity dominated. Manually identifying cluster 0 with Fp1 and cluster 1 with Fp2 (supplementary Figure 9) yielded an accuracy of 94.75%.

3 Discussion

We demonstrated that CytoNet learns cortical cytoarchitecture from large-scale histological data without requiring manual annotations. The model encodes laminar and areal organization into a feature space that generalizes across subjects, aligns with cortical morphology, and supports diverse applications including area classification, layer segmentation, structure prediction, and exploratory parcellation. In addition, CytoNet features decode widely used functional network parcellations, supporting a direct link between cellular-scale microarchitecture and macroscale functional systems. These results show that anatomical proximity provides an effective training signal, turning spatial continuity into a self-supervised objective that captures the latent factors of cortical organization. Together, they establish CytoNet as a biologically grounded and practically scalable foundation for systematic analysis of cortical histology at whole-brain scale, capable of integrating cytoarchitectonic patterns across brains while preserving both global consistency and individual variability.

The properties of the learned feature space can be traced back to the proposed SpatialNCE training strategy. SpatialNCE derives its training signal by assuming that spatially close samples are often semantically consistent. In terms of cortical organization, this translates to prior knowledge that textures observed in proximity often show architectural variations of the same functional modules. This principle distinguishes CytoNet from other self-supervised learning approaches, both contrastive (Caron et al., 2020; Chen et al., 2020; He et al., 2020; Khosla et al., 2020) and non-contrastive (Grill et al., 2020; Chen et al., 2021). It directly addresses the limitations we encountered with the SimCLR approach (Chen et al., 2020), which sometimes performed even below scratch training because it relied on augmentation-invariant confounding cues such as vascular patterns or local curvature rather than cytoarchitecture (shortcut learning, Geirhos et al. (2020)). Why, then, does augmentation-based self-supervised learning like SimCLR succeed in natural images but fail here? As argued by Kugelgen et al. (2021), augmentations implicitly define which features are treated as task-relevant *content* and which as task-irrelevant *style*. In our setting, standard augmentations (e.g., intensity distortions, noise, geometric transforms) leave confounds like vascular patterns or folding geometry intact, encouraging the model to treat them as content. This limitation reflects both the dataset and the chosen patch size: While choosing sufficiently large fields of view to capture laminar profiles inevitably includes confounds, smaller inputs could remove confounds but sacrifice important context. On the other hand, stronger augmentations (e.g., elastic deformations) may lead to undesired distortions of cytoarchitectonic structure. From this point of view, proximity-based similarity measures serve as a biologically grounded augmentation, leveraging cortical continuity across 3D space and across subjects to generate natural variations that disrupt confounds while preserving cytoarchitecture. Beyond cytoarchitecture, SpatialNCE provides an intuitive and

easy-to-use framework for multimodal self-supervision: any dataset anchored into a common spatial frame can be integrated under the same loss without modification, with only modest requirements for spatial alignment. Although demonstrated here for cortical cytoarchitecture, the principle generalizes to other domains where spatial proximity systematically relates to semantic structure (e.g., remote sensing), making it an attractive unifying paradigm for multimodal representation learning.

CytoNet’s training objective defines similarity based on the Euclidean distance between sampling locations of image patches. However, spatial coordinates are never provided as input to the model. Keeping this in mind, the organization of the learned feature space yields two key insights: First, the strong alignment between the learned feature space and anatomical location shows that local image information reliably reflects the spatial continuity of cortical organization. Second, the objective is at the same time flexible enough to deviate from this imposed geometry when needed: although its objective promotes similarity across brains, CytoNet recovers distinct brain-specific clusters with consistent internal organization. A striking example is the separation along the central sulcus: despite their adjacency in 3D space, the motor and somatosensory areas that are located anterior and posterior to the central sulcus form distinct regions in the feature space, illustrating how CytoNet recovers sharp cytoarchitectonic contrasts.

CytoNet identifies clusters with consistent internal structure within each brain, while at the same time revealing substantial differences between individuals. This pattern aligns with long-recognized interindividual variability in cytoarchitecture, first demonstrated in probabilistic maps of cytoarchitectonic areas (Amunts et al., 1999) and conceptually framed as an essential feature rather than noise in Zilles et al. (2013). Such variability can even exceed differences between areas (Amunts et al., 1999), underscoring the need to capture subject-specific patterns in cortical organization. By providing brain-specific yet systematically comparable feature spaces, CytoNet offers a computational basis for analyzing this variability at scale and relating it to functional specialization, development, and disease.

This intriguing outcome raises a key question: how can a model trained with nothing more than a proximity-based contrastive loss recover precise and meaningful anatomical structure? A likely explanation lies in the neural network architecture: projection heads in contrastive learning act as information bottlenecks, suppressing augmentation-specific signals while preserving features aligned with the loss objective (Chen et al., 2020). Consistent with this, our experiments (supplementary Section 11.2) showed that CytoNet’s projection head filters out brain-specific variation—still visible in backbone features—while preserving cytoarchitectonic structure that generalizes across subjects. However, projected features do not improve classification, indicating that the suppressed brain-specific variation is itself informative for distinguishing areas.

What exactly does CytoNet capture in its learned feature space, and how can these representations be understood? This question highlights the broader interpretability challenge that is common to deep learning methods. Classical profile-based features (Haug, 1956; Schleicher et al., 1999), including those used here as baseline for predicting structural variations (Wagstyl et al., 2018), are interpretable but also limited in scope. They mainly describe laminar intensity distributions while neglecting or oversimplifying cytoarchitectonic changes, such as cell columns, when moving across the cortical ribbon. CytoNet, in contrast, learns high-dimensional representations that encompass laminar profiles together with contextual factors such as curvature and thickness of the cortex. It also distinguishes effects of sectioning, for example different cutting angles that alter the apparent shape and size of layers and cells, and encodes approximate spatial location, which provides useful priors much like those used by human experts. The data-driven integration of these and other sources of variation in a coherent space makes it possible to dis-

ambiguate biological organization from technical influences and enables analyses that are more robust, transferable across datasets, and scalable to whole brains.

CytoNet provides a versatile foundation for automated brain mapping tasks, supporting applications such as brain area classification, cortical layer segmentation, and data-driven parcellation. Unlike earlier methods (Spitzer et al., 2018; Schiffer et al., 2021a), it generalizes across entire brains and multiple individuals without task-specific retraining, bringing fully automated mapping within reach. In our experiments, CytoNet represented the most precise method for cytoarchitectonic area classification, particularly when applied to brains without annotated training data. In practice, CytoNet outputs still require post-processing (e.g., spatial smoothing and topological constraints), but the model shifts the bottleneck from manual annotation to scalable, data-driven analysis, making it feasible to process entire brains, compare across individuals, and handle whole-brain scale datasets.

CytoNet not only outperformed existing computational methods for cytoarchitectonic area classification but also allows a valuable comparison with human expert mapping. Experts typically focus on selected areas and annotate sparsely, because their method relies on direct visual comparisons across adjacent regions to detect differences in layering and cellular composition. CytoNet, by contrast, analyzes isolated patches and scales to dozens of areas across complete brains. Both approaches, however, encounter their greatest challenges at areal borders, where cytoarchitectonic transitions follow complex and heterogeneous patterns that do not always align with sharp anatomical landmarks. Clustering experiments showed that these very transitions, while complicating border classification, can also reveal subdivisions, highlighting CytoNet’s potential for data-driven refinement. As datasets grow in resolution and size, such approaches will become increasingly important to complement expert-driven mapping. In future work, combining CytoNet with post-processing methods that enforce spatial smoothness and topological constraints (Schiffer et al., 2021b) may further enhance its utility for atlas refinement.

Classification performance dropped when CytoNet was applied to brains excluded from pretraining (i.e., to the unseen brain). This suggests that models benefit from acquiring a representational “fingerprint” for each brain. What exactly constitutes this fingerprint —individual biases in cellular biology, unknown batch effects in histological processing, or other factors—remains an important question for future work. From a practical perspective, incorporating a new brain into pretraining is not difficult: It requires only to align digitized sections approximately to the common reference space, a procedure that is well understood and supported by image registration and anchoring tools. Most importantly, no manual annotations of the images are necessary. The practicality of including each new brain in the pretraining also depends on the pace at which brain scans are typically acquired, and on the computational requirements for training. In our lab, for example, new whole-brain histological datasets are typically acquired at a pace of one or two brains per year. CytoNet would thus need to be retrained at most two times per year (requiring approximately 3600 GPU-hours), which is practically feasible on a moderately sized GPU cluster.

Complementing brain area classification, CytoNet also achieved strong performance in cortical layer segmentation, even with as little as 7 annotated image patches for training. Despite the relatively simple setup of this study (i.e., one brain, minimal training), the predictive accuracy and data efficiency suggest that the benefits of pretraining extend beyond area classification. Based on these results, we believe that CytoNet provides an important first step towards scaling automated laminar mapping —pioneered in painstaking manual studies by Brodmann (Brodmann, 1909), von Economo (Von Economo, 1925), and the Vogts (Vogt et al., 1919)— to the scale of whole brains and across individuals.

Beyond structural mapping, CytoNet features captured microarchitectural signatures of macroscale functional organization, as evidenced by high performance in predicting functional network parcellations. While functional systems exhibit strong spatial smoothness, CytoNet provided predictive information beyond what can be explained by spatial coordinates alone and exceeded established low-dimensional gradient baselines. The improved performance when combining CytoNet features with spatial coordinates suggests that cytoarchitecture and cortical position contribute complementary signals. This result supports the view that cellular architecture provides a substrate for systems-level functional differentiation (Mesulam, 1998; Hilgetag et al., 2016) and motivates future work integrating microarchitectural and neuroimaging foundation models in a common representational space.

In summary, CytoNet represents a step towards a new generation of approaches to study brain organization that are: (i) anatomically rooted, capturing fundamental structural principles, (ii) scalable, enabling dense and reproducible mapping across whole brains, (iii) general, applicable across regions, subjects, and imaging modalities, and (iv) extensible, providing a foundation for multimodal integration and holistic models of brain organization.

4 Methods

4.1 Microscopic images of histological human brain sections

The analyses were conducted using 4654 cell-body stained histological sections from ten post-mortem human brains (465 ± 19 sections/brain, min 438, max 492) from the brain collections of our laboratories in Jülich and Düsseldorf, with a total dataset size of approximately 10.71 terabytes. The processing protocol is detailed in Amunts et al. (2020) and briefly summarized in the following.

Brains were removed from the skull 24-36 hours after death (ethics approval #4863). They were chemically fixated with formalin or Bodian, and embedded in paraffin. Coronal sectioning resulted in 6000-7500 histological sections with 20 μm thickness. Every 15th section (every section for B20) was mounted on a glass slide and stained for neuronal cell bodies using a modified silver staining (Merker, 1983). Sections were then digitized using high-throughput light-microscopic scanners (TissueScope HS, Huron Digital Pathology Inc.) at a resolution of 1 $\mu\text{m}/\text{px}$. Resulting images have a median size of 77,000 px \times 105,000 px (7.5 GB), with a maximum size of up to 95,000 px \times 136,000 px (12 GB). Brain samples have the following numerical identifiers: B01, B03, B04, B05, B06, B07, B09, B10, B12, and B20. Brain sections are referred to by four-digit numbers that increase along the posterior-anterior axis. Brain B20 refers to the so-called BigBrain model, a 3D-reconstructed dataset based on 7404 histological sections (Amunts et al., 2020). To be comparable with the other nine brains, every 15th section of B20 was used in this study.

4.2 Generation of sampling locations in the cerebral cortex

A dataset for contrastive pretraining of CytoNet was prepared by defining sampling locations along the cortical midline in all brains. The cortical midline runs centered between the pial surface and the gray matter surface. Identifying the cortical midline based on 2D scans of histological sections is sometimes challenging due to the projection of the three-dimensional structure of the cortex onto the 2D image planes. To address this, each brain was approximately

3D reconstructed by section-to-section alignment, consistent midsurfaces in 3D were computed, and then projected back onto the 2D image planes ².

Approximate 3D reconstructions of all brains were computed, except for brain B20, for which the high-resolution anatomical reconstruction of the BigBrain dataset was used. Reconstructions were created by computing rigid alignments between all pairs of adjacent brain sections (Dickscheid et al., 2019). Rigid transformations were estimated from SURF features (Bay et al., 2006) computed at a resolution of 64 $\mu\text{m}/\text{px}$, which were matched using k-nearest neighbor matching and filtered by the RANSAC algorithm (Fischler et al., 1981). For a few sections, rigid alignment was not sufficient because these sections were digitized with reversed orientation, producing left–right mirrored images. Affine transformations for these sections were computed after identifying them in a manual quality check. Finally, the approximate 3D reconstruction of each brain was computed by aligning all sections to a base section in the center of the section stack of each brain using recursive application of the computed section-to-section transformations. Limiting the alignment to rigid transformations avoids strong deformations and distortion of the reconstructed brain volumes.

To compute cortical midsurfaces, each section image was segmented ³ into gray matter, white matter, and background (i.e., microscopy slide). Microscopic scans downsampled to 64 $\mu\text{m}/\text{px}$ were used for computing this tissue segmentation. Before segmentation, the contrast of the images was enhanced to better distinguish between gray and white matter. A minimum filter, a maximum filter, and a mean filter were applied, each with size 5. In a next step, the contrast was enhanced using contrast limited adaptive histogram equalization (CLAHE, Pizer et al. (1987)) with a kernel size of 250, followed by Gaussian blurring (standard deviation 1), followed by another round of minimum, maximum, and mean filters with size 5. The background class was identified by searching for local minima in the intensity histogram (256 bins) of each image. Histograms were smoothed using a median filter (size 3) and a mean filter (size 5) to make the process robust against noise. If more than one minimum was found, the one closest to the Otsu threshold (Otsu, 1979) was used. Pixels identified as tissue using the background segmentation were segmented into gray and white matter using morphological active contours (Márquez-Neila et al., 2014), a variant of the Chan-Vese segmentation method (Chan et al., 1999). Resulting segmentations were cleaned using morphological operations to remove small objects and holes from the mask. All steps were tuned to prevent tight sulci from being closed during segmentation or cleanup to retain the shape of the cortex. Obtained segmentation masks were then 3D reconstructed at an isotropic resolution of 300 $\mu\text{m}/\text{vx}$ using the computed rigid transformations. For B20, the tissue segmentation available from the BigBrain dataset was used (Lewis et al., 2014).

These segmentation volumes were cleaned to remove segmentation errors, imprecise alignment, or histological artifacts. Tissue defects were detected by smoothing volumes with a median filter of size 3 in the posterior-anterior direction and computing the difference to the input volume. Larger tissue defects were identified by detecting large connected components in the difference volume, and then replaced by the result of the median filter. Small parts of detached tissue were removed by extracting all connected components that were smaller than 1% of the largest tissue component. Parts of the volume belonging to subcortical gray matter and the cerebellum, which are not handled by the employed segmentation pipeline, were manually identified and excluded using the *3DSlicer* software (Kikinis et al., 2014). The manual steps required approximately 30 min per brain.

²Code available at https://jugit.fz-juelich.de/inm-1/bda/software/data_processing/brain3d.

³Code available at <https://jugit.fz-juelich.de/inm-1/bda/software/analysis/tseg>.

Following Leprince et al. (2015), the Laplacian field in the cerebral cortex was computed using *BrainVisa* (Rivière et al., 2009). The Laplacian field approximates the cortical depth, taking the value 0 at the pial surface and linearly increasing to 1 towards the gray-white matter boundary. The *marching cubes algorithm* (Lewiner et al., 2003) was applied to extract the 0.5-isosurface from the Laplacian field, which approximates the midsurface through the cortex. The resulting midsurface meshes were cleaned by removing small isolated connected components, splitting brain hemispheres into separate meshes, fixing topological errors, and computing a Poisson surface reconstruction (Kazhdan et al., 2006) to remove artifacts from reconstruction inaccuracies or segmentation errors. Isotropic explicit remeshing (Surazhsky et al., 2003) was then applied to remesh all triangle edges to a length of approximately 300 μm . Mesh processing was performed using the *MeshLab* software (Cignoni et al., 2008).

The 2D midline through the cortex was derived by projecting the 3D midsurface back onto the 2D images. For each histological section, the plane that cuts through the midsurface at the location of the respective brain section was determined, and the intersection between this plane and the midsurface, which can be interpreted as “virtually cutting” the reconstructed brain, was computed. The intersection was transformed back onto the brain sections by inverting the transformations used for 3D reconstruction.

As a result of the smoothing and cleaning steps in 3D, points transformed from 3D to 2D were not always located exactly in the center of the cortex. To address this, a refinement step that “pushes” points towards the cortical midline was applied. For the refinement, the morphological skeleton of the cortex segmentations was derived. Laplacian fields between the skeleton and both the pial boundary and gray-white matter boundary were then computed using successive over-relaxation. Each point was then integrated through the gradient field of the Laplacian fields, limiting the maximum movement to 2 mm. Points that contained less than 50% tissue according to the tissue segmentation were excluded from further processing. In total, 4,546,775 sample points were created ($454,678 \pm 44,339$ points/brain, min 399,493, max 539,030).

During pretraining, the presented SpatialNCE loss requires each image patch to be associated with a corresponding spatial location in the brain for computing similarity between samples. To allow distance computation across brains, it is important for spatial locations to be defined in a common reference coordinate system. To accomplish this, we made use of the fact that digitized histological sections used for training CytoNet are a subset of the dataset that was used to create the Julich Brain Atlas (Amunts et al., 2020), for which linear and non-linear transformations from the pixel space of the digitized histological sections and the individual brain template *MNI Colin 27* (Holmes et al., 1998) are available as part of the Julich Brain workflow. These transformations were used to associate each sampling location in the microscopic images with a corresponding location in the coordinate system of the MNI Colin 27 space. Details on the used transformation workflow are provided in Amunts et al. (2020). In supplementary Section 11.4, we additionally evaluated models pretrained on coordinates from the *MNI 152 ICBM 2009c Nonlinear Asymmetric template space* (Fonov et al., 2011), obtained by nonlinearly transforming coordinates from MNI Colin 27 space using *siibra-python* (Dickscheid et al., 2025).

4.3 Deep neural network architectures

CytoNet was evaluated with two architecture variants: *R50* and *R50-ViT*. *R50* is a modified ResNet50 (He et al., 2016) architecture following Schiffer et al. (2021a), where the initial down-sampling block (i.e., the first two convolutional layers and the pooling layer) is replaced with two convolutional layers (5×5 convolution with stride 4 and 3×3 convolution with stride 1, 64

filters each) and a 2×2 maximum pooling operation to account for the significantly larger input image size compared to many other classification tasks. Each convolutional layer is followed by a batch normalization layer (Ioffe et al., 2015) and ReLU activation.

R50-ViT is a hybrid between *R50* and the *ViT-B* vision transformer architecture (Dosovitskiy et al., 2020), which is constructed by appending a *ViT-B* vision transformer to the feature map produced by *R50*. The transformer uses learned positional embeddings that are added to the incoming feature maps. A special class token is prepended to the transformer input sequence, which aggregates information from the entire input image. See He et al. (2016) and Dosovitskiy et al. (2020) for an in-depth description of the ResNet50 and ViT-B neural network architectures, respectively.

Models trained using these architectures are referred to by a combination of the training paradigm, the model architecture, and the number of pretraining samples (if applicable). For brevity, the R50 part is omitted, as all evaluated models are either pure R50 architectures, or hybrids of R50 and ViT-B. For example, *scratch* refers to a model trained from scratch using the R50 architecture, *SubCon-ViT* refers to a model trained using supervised contrastive learning with the R50-ViT-B hybrid architecture, and *CytoNet (1M)* refers to CytoNet pretrained on 1 million samples using R50 architecture.

4.4 Self-supervised pretraining of CytoNet

Dataset. Two pretraining datasets were created by randomly sampling 200,000 and 1,000,000 samples from all generated sampling locations (Section 4.2), denoted as *200k* and *1M*, respectively. No balancing of samples (e.g., to address varying area sizes) was performed. During training, microscopic image patches were extracted centered at the sampled locations. Each image patch had a square size of 2,048 px at a resolution of $2 \mu\text{m}/\text{px}$, resulting in an effective field of view of approximately 4mm . According to Von Economo (1925), cortical thickness in the isocortex (before correction for shrinking from histological processing) varies between 3.3 to 4.5 mm in the primary motor cortex (Brodmann area 4) and 1.9 to 2.1 mm in the primary somatosensory cortex (Brodmann area 3). The field of view is thus sufficiently large to fully capture cytoarchitectonic patterns in most parts of the isocortex.

Training protocol. CytoNet was trained using Stochastic Gradient Descent (SGD) with Nesterov momentum and a momentum factor of 0.9 in combination with the LARS optimizer (You et al., 2017) with trust coefficient 0.02. The batch size was $B = 2048$, and the learning rate was set to $0.01 * (B/256) = 0.08$, which was kept constant over the course of the training. Weight decay with a factor of 0.0001 was applied to all non-bias parameters of the model. The temperature parameter τ for contrastive pretraining was set to 0.07. Pretraining was performed for 150 epochs. The RBF kernel for the SpatialNCE loss used a bandwidth of $\sigma = 10 \text{ mm}$.

Data augmentation was applied to capture typical variations in the data, following the data augmentation strategy detailed in Schiffer et al. (2021a), which is briefly summarized below. Image patches were randomly rotated by $\theta \sim U[-\pi, +\pi]$ ($U[a, b]$: uniform distribution over $[a, b]$), patch center positions were translated in a random direction by $d \sim U[0\text{mm}, 0.2\text{mm}]$, and mirrored vertically with a probability of 50%. Pixel intensities $x \in [0, 1]$ were randomly augmented using unbiased gamma augmentation (Pohlen et al., 2017) $\alpha x^\gamma + \beta$ with parameters $\alpha \sim U[0.9, 1.1]$, $\beta \sim U[-0.1, +0.1]$, $\gamma = \frac{\log(0.5+2^{-0.5}Z)}{\log(0.5-2^{-0.5}Z)}$, $Z \sim U[-0.05, +0.05]$. In addition, images were blurred with an isotropic Gaussian $G_\sigma(x)$ of kernel size $\sigma \sim U[0.125, 1.0]$, or sharpened

according to $x + \delta(G_{\sigma_u}(x) - x)$ with $\sigma_u \sim U[0.125, 1.0]$, $\delta \sim U[0.5, 1.5]$ with probability 25%, respectively. After augmentation, images were standardized to $[-1, 1]$ before being passed into the model.

Following Chen et al. (2020), projection layers were attached to the respective backbone architecture and the contrastive loss was computed on the output of the projection layers. A fully-connected layer with as many hidden units as the respective backbone output (2048 for R50; 768 for R50-ViT), batch normalization (Ioffe et al., 2015), ReLU, and a final linear layer with 256 units were applied to the output of global average pooling for *R50* or the class token for *R50-ViT*.

4.5 Brain area classification

Dataset. The dataset used to train classifiers for 113 cytoarchitectonic areas was derived from annotations shown in the Julich Brain atlas (version 3.1, both hemispheres, Amunts et al. (2020)), following the protocol described in Schiffer et al. (2021a). The list of areas is provided in supplementary Table 2. Annotations were available as contours outlining the outer boundaries of each area. To generate sampling locations for extracting image patches, the cortical midline was first computed from the morphological skeleton of the rasterized contours. Sampling points were then uniformly spaced along this midline at 1 mm intervals.

From these potential sampling points, datasets for training, testing, and transferability evaluation were created. Brains were grouped into three categories —*seen brains*, *transfer brains*, and *unseen brains*— based on their inclusion in (i) self-supervised pretraining (if applicable) and (ii) supervised training for brain area classification. Our default configuration for these datasets is shown in Table 1. Brains were randomly assigned to one of the three categories.

Sections from *seen brains* were divided into training and test sections, with 80% used for supervised training and 20% reserved for testing. Test sections were selected by choosing every fifth annotated section from each brain. This setup reflects a realistic use case in which models are applied to new sections from a brain with existing partial annotations.

Transfer brains were included in self-supervised pretraining but excluded from supervised training. This configuration enables evaluation of how well the learned representations transfer to brains without annotated training data, a common scenario in ongoing brain mapping efforts where new brains are digitized but not yet manually labeled.

Unseen brains were excluded from both self-supervised and supervised training. This strict separation provides a measure of generalization to entirely novel brains.

To address class imbalance in the training set —caused by variations in the size of cytoarchitectonic areas— stratified sampling with replacement was applied. For each area, 1200 image patches were sampled, resulting in a balanced training set of 135,600 patches. The sampling rate was chosen such that the median ratio between sampled and available patches across all areas was close to 1. Test datasets were not resampled and reflect the natural distribution of area sizes.

Training protocol. Models were trained to classify 113 cytoarchitectonic brain areas by attaching a linear classifier to R50 or R50-ViT architectures (Section 4.3). Projection layers from pretrained models were discarded and replaced with a single linear layer (without bias) consisting of 113 output units. This classifier was attached to the global average pooling output (for R50) or the class token (for R50-ViT). Several baseline models were compared to CytoNet:

- **Training from scratch:** full supervised training from randomly initialized weights.

Table 1: Brains used for pretraining, linear probing and finetuning.

dataset	brain(s)	pretraining	supervised training
seen brains	B01, B03, B04, B05 B06, B10, B12, B20	✓	✓
transfer brain	B07	✓	✗
unseen brain	B09	✗	✗

- **Supervised contrastive learning (SupCon)** (Khosla et al., 2020; Schiffer et al., 2021a): supervised contrastive pretraining on labeled training samples.
- **SimCLR (200k and 1M)** (Chen et al., 2021): self-supervised pretraining from semantic consistency under multi-view augmentation.
- **CytoNet (200k and 1M)**: self-supervised pretraining from spatial consistency in 3D space using SpatialNCE loss.

Classifier training for pretrained models (SupCon, SimCLR, CytoNet) was performed for 30 epochs, while training from scratch was performed for 180 epochs. Note that the number of epochs is not directly comparable across all models, since training from scratch and SupCon pretraining are limited to annotated samples, while SimCLR and CytoNet make use of unannotated samples as well. Nevertheless, the chosen number of epochs was sufficient to ensure convergence in both pretraining and supervised training.

For all models, two training strategies were evaluated:

- **Linear probing:** Only the classifier was trained, while the pretrained backbone and corresponding batch normalization statistics remained frozen. Note that this setting is not applicable for training from scratch.
- **Finetuning:** Both the classifier and backbone weights were optimized jointly.

All models were trained using categorical cross-entropy loss and the same data augmentation protocol as used during CytoNet pretraining (Section 4.4).

Unless otherwise noted, models were trained using SGD with Nesterov momentum and a scaled learning rate of $0.01 \times (B/256) = 0.08$, with batch size $B = 2048$, and weight decay of 0.0001 applied to all non-bias parameters. Model-specific adjustments were necessary to stabilize training and included:

- **scratch-ViT** and **CytoNet-ViT (200k)**: learning rate reduced to 0.008.
- **SupCon-ViT**: trained with AdamW and learning rate 0.001.

To evaluate the effect of the projection layer, we also trained and tested a variant of CytoNet-ViT (1M), denoted as *CytoNet-ViT (1M) P*, where the classifier was attached to the output of the pretrained projection layer. Both linear probing and finetuning were performed to assess whether the projected feature space contains sufficient task-relevant information.

4.6 Cortical layer segmentation

Dataset. For cortical layer segmentation, a dataset of 913 high-resolution microscopic image patches at $1\ \mu\text{m}/\text{px}$ resolution was used, each manually annotated with segmentation masks for the six cortical layers as well as background (see Figure 6, B). The dataset extends a publicly available resource described in Dickscheid et al. (2021). To match the resolution used during CytoNet and baseline pretraining, images were downsampled to $2\ \mu\text{m}/\text{px}$, and segmentation masks were rescaled to 32×32 pixels ($128\ \mu\text{m}/\text{px}$) to match the output resolution of our models. Irregularly shaped patches were converted to square format using mirror padding to ensure compatibility with the model input size.

The dataset was split into a fixed 80-20 split (732 training and 184 test patches). To simulate varying annotation budgets, 1%, 5%, 10%, 20%, and 100% subsets of the training pool were sampled. Each training subset was further split into five folds. For each fold, a model was trained and then evaluated on the fixed test set. This repeated sampling design allowed estimating the stability of model performance across different training subsets of equal size. All results are reported on the held-out test set. Mean and standard deviation of class-wise macro-F1 scores across the five trained models for each configuration are reported. To ensure a fair evaluation, mirror padding used to make irregularly shaped images compatible with the models was removed before computing scores.

Training protocol. Models were trained to classify the layer structure of the isocortex by attaching a pixel-wise linear classifier to R50 or R50-ViT architectures (Section 4.3). Projection layers from pretrained models were discarded and replaced with a 1×1 convolutional layer (without bias) with 7 channels (six layers plus background). This classifier was attached to the global average pooling output (for R50) or the class token (for R50-ViT). Similar to brain area classification (Section 4.5), training from scratch, SimCLR (200k and 1M) (Chen et al., 2021), and CytoNet (200k and 1M) were compared, each trained using linear probing and finetuning. All models used either R50 or R50-ViT architectures, AdmaW optimizer with a learning rate of 0.001 and weight decay of 0.01, and categorical cross-entropy loss. No data augmentation was applied during training.

4.7 Predicting structural variations in cytoarchitecture

Extraction of morphological features from BigBrain. Morphological features for brain B20 were extracted using the 3D reconstruction of the BigBrain dataset (Amunts et al., 2020). Cortical curvature was computed using the *highres-cortex* (Leprince et al., 2015) module of the *BrainVisa* software (Rivière et al., 2009) based on the gray-white matter segmentation available through the *siibra tool suite* (Dickscheid et al., 2025). To assess the cutting direction, the angle between the histological cutting plane and the cortical surface normal was measured. Surface normals were approximated by computing the gradient of a Laplace field defined between the pial surface and the gray-white matter boundary. The cutting direction was then quantified as the angle between these gradient vectors and the anterior-posterior axis, which corresponds to the histological cutting direction in BigBrain. Low angles indicate near-orthogonal slicing relative to the cortical sheet, whereas high angles reflect more oblique cuts, which can obscure the cortical lamination pattern (Schleicher et al., 1999). Cortical thickness and layer-specific thicknesses (layers I–VI) were obtained from surface meshes described in Wagstyl et al. (2020), accessible via the *siibra* suite. Thickness was computed as the Euclidean distance between corresponding mesh vertices across laminar surfaces and mapped to the closest points on the

cortical midline. Finally, computed features were assigned to points sampled along the cerebral cortex (Section 4.2) based on location in BigBrain space. All computed features were assigned to sampled cortical points (Section 4.2) based on their coordinates in BigBrain space.

Extraction of layer-wise cell-density from microscopic image patches. Layer-wise average cell densities were computed from the cortical image patches described in Section 4.6. For each patch cell density was estimated using a kernel density estimator with a kernel bandwidth of 100 μm , based on the positions of segmented cell bodies (Upschulte et al., 2022). The resulting density maps were then averaged within each cortical layer, yielding one average cell density value per layer and patch.

BigBrain intensity profiles. Intensity profiles (Wagstyl et al., 2022) sampled across the BigBrain dataset (Amunts et al., 2013) capture depth-dependent structural variations by measuring pixel intensity gradients across the cortical sheet. A publicly available dataset from Wagstyl et al. (2022) was used, comprising 327684 cortical profiles. Each profile contains 200 equidistant intensity values sampled along a 1-pixel wide line perpendicular to the cortical surface, extending from the pial boundary to the gray–white matter interface. Prior to correlation analysis, all intensity values were standardized via z-scoring.

Correlative analysis of CytoNet features and BigBrain intensity profiles. We conducted a correlative analysis between feature embeddings and known morphological and structural properties of the cerebral cortex. Learned feature representations of CytoNet-ViT (1M) were compared with structural features extracted from brain B20, including cortical curvature, cortical thickness, layer-specific thickness, cutting direction, and layer-wise cell densities. In parallel, we conducted the same analysis using depth-wise intensity profiles (see above) to serve as a baseline for comparison.

For both CytoNet features and intensity profiles, correlations against all target features were evaluated using two input feature sets: the raw features, and principal component projections with dimensionalities 1, 16, 32, 64, 128, and 256. Principal component analysis (PCA) was fitted once on the entire dataset and applied consistently across all folds. To quantify predictive strength, separate linear regression models for each target feature were trained. Models were evaluated using five-fold cross-validation, with R^2 scores computed on the held-out test folds and reported as mean \pm standard deviation across folds. All regressions were implemented using *scikit-learn* with default hyperparameters. R^2 scores for the prediction of layer-wise cell density using CytoNet features are not available, as the number of samples in each fold (730) was not sufficient to fit a linear classifier based on all dimensions of the CytoNet features (768).

To further interpret the latent structure of CytoNet representations, feature attribution was performed for the first 16 principal components of the CytoNet feature space. Linear attribution weights were computed by fitting a separate linear regressor to each target property and normalizing the regression coefficients by the ratio of input to output standard deviation. This normalization ensures that attributions are comparable across targets with differing dynamic ranges.

To evaluate the generalizability of spatial encoding in CytoNet representations, regressors were trained on data from brain B20 and applied to spatial locations in other brains (supplementary Table 4). No finetuning or domain adaptation was performed across brains in this analysis.

4.8 Decoding functional organization from cytoarchitecture

We evaluated whether CytoNet representations can decode macroscale functional organization on the cortical surface. CytoNet-ViT (1M) features were computed for BigBrain B20, assigned to the BigBrain midsurface by nearest-neighbor lookup in 3D coordinate space, and mapped to fs_LR surface space for all decoding analyses.

As functional targets, we used the Yeo7 and Yeo17 network parcellations (Yeo et al., 2011) as well as the DiFuMo atlas with 64 functional modes (Dadi et al., 2020). Yeo labels were obtained in BigBrain space from the *BigBrainWarp* toolbox (Paquola et al., 2021). DiFuMo64 was fetched in MNI152 space using the *sibra* tool suite (Dickscheid et al., 2025) and mapped to fs_LR (32k) surface space (Van Essen et al., 2012) with nearest-neighbor resampling using *neuromaps* (Markello et al., 2022).

All experiments were performed in fs_LR (32k) surface space after mapping all features and targets to this space. CytoNet feature maps were warped from BigBrain space to fs_LR using *BigBrainWarp*. For baseline comparisons, we additionally included histological gradients (Hist-G1 and Hist-G2) (Paquola et al., 2019), microstructural gradients derived from qT1 (Micro-G1 and Micro-G2) (Royer et al., 2022), and functional gradients (Func-G1 and Func-G2) (Margulies et al., 2016), obtained via *BigBrainWarp* and evaluated in the same fs_LR space. We also evaluated a spatial baseline using fs_LR vertex coordinates (x,y,z), and a combined feature set concatenating CytoNet PCA features with coordinates.

To obtain low-dimensional CytoNet variants, principal component analysis (PCA) was fitted once on CytoNet features pooled across both hemispheres in fs_LR space and subsequently applied to each hemisphere. We evaluated PCA projections with 1, 2, and 32 components.

Functional labels were predicted using multinomial logistic regression with class balancing, implemented in *scikit-learn*. All input features were standardized within each training fold (zero mean, unit variance) and the transformation was applied to the held-out fold.

Spatially grouped cross-validation. To reduce score inflation from spatial autocorrelation, we used grouped 5-fold cross-validation with groups defined by spatial surface superblocks. Superblocks were generated by 3-fold explicit isotropic mesh decimation of the fs_LR surface to obtain a coarser set of vertices, assigning each original vertex to its nearest remeshed vertex, and then clustering block centroids into 100 parcels per hemisphere using *k*-means. All vertices belonging to the same superblock were kept in the same fold.

Spin-based spatial null. To test whether performance gains over the coordinate baseline can be explained by spatial smoothness alone, we performed a spin-based spatial permutation test on the Yeo labels in fs_LR space. For each hemisphere, labels were rotated on the spherical fs_LR representation using random rotations and reassigned to vertices by nearest-neighbor matching on the sphere, implemented with *neuromaps* (Markello et al., 2022). Rotations were performed independently per hemisphere to preserve hemispheric topology, and the same spatially grouped cross-validation procedure was applied after each spin. We assessed statistical significance of the observed improvement in macro-F1 between CytoNet PCA-32 and the coordinate-only baseline using a one-sided test, with $p = (1 + \#\{\Delta_{\text{spin}} \geq \Delta_{\text{obs}}\}) / (1 + N_{\text{spin}})$. When testing multiple parcellations, *p*-values were corrected using Holm–Bonferroni. Performance was quantified by macro-F1 and reported as mean \pm standard deviation across spatially grouped cross-validation folds. To reduce runtime, spin tests were conducted in parallel using 1024 CPU cores across

4 compute nodes of JURECA-DC (runtime Yeo7: 18 minutes; Yeo17: 43 minutes; DiFuMo64: 160 minutes).

4.9 Data-driven mapping of cortical areas

Dataset. We assessed whether CytoNet feature embeddings support data-driven subdivision of cortical areas by focusing on the frontal pole regions Fp1 and Fp2 (Bludau et al., 2014) in B06. These two areas form subdivisions of Brodmann area 10 and are located in the anterior portion of the prefrontal cortex. To pre-localize the region of interest, two complementary sources of anatomical information with different levels of spatial precision were used: (1) image-level annotations of Fp1 and Fp2 from Bludau et al. (2014), and (2) probabilistic maps for the same areas provided by the Julich Brain Atlas 3.1 (Amunts et al., 2020). Cortical sampling points were generated along the midline as described in Section 4.2, without spatial subsampling. Each point was assigned both a discrete label based on the image-level annotations and a probabilistic value from the atlas maps.

Clustering. k -means clustering was used to evaluate whether CytoNet feature representations can differentiate between areas Fp1 and Fp2 of the frontal pole (Bludau et al., 2014). CytoNet features were extracted from the backbone of the trained R50-ViT (1M) model, prior to the final projection head, and used directly without PCA or normalization. Clustering was performed separately for two subsets of cortical points, corresponding to the two pre-localization strategies.

For the atlas-based approach, all points with a probability greater than 50% of belonging to either Fp1 or Fp2 were selected. These points were clustered into $k = 6$ groups to account for the spatial uncertainty and potential heterogeneity of the probabilistic maps.

For the annotation-based approach, only points that were explicitly labeled as Fp1 or Fp2 were selected. These were clustered into $k = 2$ groups to match the number of known areas and to simulate the task of deciding whether a previously identified region should be subdivided.

In both settings, clustering was performed across points from both hemispheres using Euclidean distance in the CytoNet feature space. No feature normalization or spatial smoothing was applied prior to clustering. Cluster identity was not constrained by anatomical proximity or continuity. The consistency of cluster-to-label alignment was quantified using cluster purity. The purity of a cluster is defined as the fraction of its samples belonging to the most frequent ground truth label. For each clustering run, the mean purity across all clusters was computed. The overall clustering performance is reported as the mean and standard deviation of these average purities across 30 runs.

4.10 Computational setup

CytoNet pretraining (Section 4.4) and linear probing for brain area classification (Section 4.5) were performed on 16 compute nodes of the supercomputer *JURECA-DC* (Thörnig, 2021) at Jülich Supercomputing Centre (JSC, Forschungszentrum Jülich, Jülich, Germany). Each compute node was equipped with four Nvidia A100 GPUs (4×6912 CUDA cores, 4×432 tensor cores, $4 \times 40GB$ HBM2e memory), two AMD EPIC 7742, 2×64 cores à 2.5GHz with hyperthreading, 512 GB memory, and InfiniBand HDR100 interconnect. Training, inference, and evaluation were implemented using *ATLAS*⁴, a Python framework that enables large-scale neural network training for high-resolution microscopic image data.

⁴<https://jugit.fz-juelich.de/inm-1/bda/software/analysis/atlas/atlas>

ATLaS uses PyTorch (Paszke et al., 2019) for neural network training. Training was parallelized using distributed data parallel (DDP) training, where each GPU processes a subset of samples in each batch and averages gradients before applying parameter updates. During contrastive pretraining, features computed by each GPU were gathered to compute pairwise similarities across all samples of a batch. Statistics computed by batch normalization layers were synchronized across GPUs in each training step. Automatic Mixed Precision (AMP) was applied to improve training performance by computing certain compute operations with reduced floating point precision. Gradient checkpointing was used for training R50-ViT models, setting checkpoints after all residual blocks of the convolutional network except for the first one, as well as all transformer layers. The average GPU memory footprint during contrastive pretraining (32 samples per GPU) was 37.6 GiB for *R50* and 34.4 GiB for *R50-ViT* (with gradient checkpointing). Pretraining (Section 4.4) on 1 million samples for 150 epochs took approximately 28h (1792 GPU hours, 75 GPU days). Linear probing or finetuning for brain area classification (Section 4.5) on 131250 samples for 30 epochs took approximately 1.5 hours (96 GPU hours, 4 GPU days).

Training of models for cortical layer segmentation was performed on a workstation equipped with an Nvidia RTX 4090 GPU (24 GB RAM), Intel i9-14900k (32 cores à 6 GHz), and 192 GB RAM, taking between 5 minutes and 40 minutes per fold, depending on the fraction of used training samples, the model architecture, and whether linear probing or finetuning was used. The linear regression of structural variations (Section 4.7) was performed on the same workstation, taking up to 30 seconds per fold, depending on the dimensionality of the input vectors. No GPU acceleration was used for linear regression.

5 Acknowledgement

This project received funding from the European Union’s Horizon 2020 Research and Innovation Programme, grant agreement 101147319 (EBRAINS 2.0 Project), the Helmholtz Association port-folio theme “Supercomputing and Modeling for the Human Brain”, the Helmholtz Association’s Initiative and Networking Fund through the Helmholtz International BigBrain Analytics and Learning Laboratory (HIBALL) under the Helmholtz International Lab grant agreement InterLabs-0015, from HELMHOLTZ IMAGING, a platform of the Helmholtz Information & Data Science Incubator [X-BRAIN, grant number: ZT-I-PF-4-061], and from the Deutsche Forschungsgemeinschaft (DFG, German Research Foundation) under the National Research Data Infrastructure – NFDI 46/1 – 501864659. Computing time was granted through JARA on the supercomputer JURECA-DC at Jülich Supercomputing Centre (JSC).

6 Author contributions

CS: Conceptualization, Data curation, Formal analysis, Funding acquisition, Investigation, Methodology, Project administration, Software, Validation, Visualization, Writing – original draft. **ZB:** Methodology, Software, Writing – review & editing. **JK:** Methodology, Software, Validation, Writing – review & editing. **JT:** Data curation, Methodology, Software, Writing – review & editing. **KB:** Formal analysis, Investigation, Validation, Writing – review & editing. **HS:** Methodology, Investigation, Validation, Software, Writing – review & editing. **KA:** Conceptualization, Funding acquisition, Methodology, Project administration, Resources, Supervision, Validation, Writing – review & editing. **TD:** Conceptualization, Funding acquisition,

Methodology, Project administration, Software, Supervision, Validation, Writing – review & editing.

7 Declaration of Interests

The authors declare no competing interests.

8 Declaration of generative AI and AI-assisted technologies in the writing process

During the preparation of this work the authors used ChatGPT (versions 5.0 and 5.1) in order to improve the clarity and brevity of the text. After using this tool, the author(s) reviewed and edited the content as needed and take full responsibility for the content of the published article.

9 Ethics declaration

The presented study requires no separate ethical approvals. All usage in this work is covered by a vote of the ethics committee of the Medical Faculty of the Heinrich Heine University Düsseldorf (#4863). Postmortem brains were obtained through body donor programs of the anatomical institutes of the universities of Düsseldorf, Rostock, and Aachen, in accordance with legal and ethical regulations and guidelines. All body donors have signed a declaration of agreement.

10 Data and code availability

1. All source code is publicly available under Apache 2.0 licence. The source code used for model training and evaluation is available at <https://jugit.fz-juelich.de/inm-1/bda/software/analysis/atlas/atlas>. A docker container for reproducible execution is provided at https://jugit.fz-juelich.de/inm-1/bda/software/analysis/atlas/atlas_container. Trained model weights, corresponding configuration files, and feature embeddings are available at https://jugit.fz-juelich.de/inm-1/bda/software/analysis/cytonet_model_zoo. Code for approximate 3D reconstructions is available at https://jugit.fz-juelich.de/inm-1/bda/software/data_processing/brain3d. Code for tissue segmentation is available at <https://jugit.fz-juelich.de/inm-1/bda/software/analysis/tseg>.
2. The full histological image dataset used in this study cannot yet be deposited in a public repository because of ongoing processing, data curation, and setup of suitable technical infrastructure to host the dataset. To request access, contact Katrin Amunts (k.amunts@fz-juelich.de, Forschungszentrum Jülich, Germany) with a summary of the planned study. In addition, representative sections of B20 are accessible via the EBRAINS Knowledge Graph (<https://doi.org/10.25493/JWTF-PAB>).
3. Interactive versions of selected figures are available at <https://go.fzj.de/cytonet-interactive>.

References

- Amunts, K., J. DeFelipe, C. Pennartz, A. Destexhe, M. Migliore, P. Ryvlin, S. Furber, A. Knoll, L. Bitsch, J. G. Bjaalie, Y. Ioannidis, T. Lippert, M. V. Sanchez-Vives, R. Goebel, and V. Jirsa (2022). “Linking Brain Structure, Activity, and Cognitive Function through Computation”. In: *eNeuro* 9.2. DOI: 10.1523/ENEURO.0316-21.2022.
- Amunts, K., C. Lepage, L. Borgeat, H. Mohlberg, T. Dickscheid, M.-É. Rousseau, S. Bludau, P.-L. Bazin, L. B. Lewis, A.-M. Oros-Peusquens, N. J. Shah, T. Lippert, K. Zilles, and A. C. Evans (2013). “BigBrain: An Ultrahigh-Resolution 3D Human Brain Model”. In: *Science* 340.6139, pp. 1472–1475. DOI: 10.1126/science.1235381.
- Amunts, K. and T. Lippert (2021). “Brain Research Challenges Supercomputing”. In: *Science* 374.6571, pp. 1054–1055. DOI: 10.1126/science.ab18519.
- Amunts, K., A. Malikovic, H. Mohlberg, T. Schormann, and K. Zilles (2000). “Brodmann’s Areas 17 and 18 Brought into Stereotaxic Space —Where and How Variable?” In: *NeuroImage* 11.1, pp. 66–84. DOI: 10.1006/nimg.1999.0516.
- Amunts, K., H. Mohlberg, S. Bludau, and K. Zilles (2020). “Julich-Brain: A 3D Probabilistic Atlas of the Human Brain’s Cytoarchitecture”. In: *Science* 369.6506, p. 988. DOI: 10.1126/science.abb4588.
- Amunts, K., A. Schleicher, U. Bürgel, H. Mohlberg, H. B. M. Uylings, and K. Zilles (1999). “Broca’s Region Revisited: Cytoarchitecture and Intersubject Variability”. In: *Journal of Comparative Neurology* 412.2, pp. 319–341. DOI: 10.1002/(SICI)1096-9861(19990920)412:2<319::AID-CNE10>3.0.CO;2-7.
- Amunts, K. and K. Zilles (2015). “Architectonic Mapping of the Human Brain beyond Brodmann”. In: *Neuron* 88.6, pp. 1086–1107. DOI: 10.1016/j.neuron.2015.12.001.
- Amunts, K. et al. (2024). “The Coming Decade of Digital Brain Research: A Vision for Neuroscience at the Intersection of Technology and Computing”. In: *Imaging Neuroscience* 2, imag-2-00137. DOI: 10.1162/imag_a_00137.
- Bardes, A., J. Ponce, and Y. LeCun (2022). “VICReg: Variance-Invariance-Covariance Regularization for Self-Supervised Learning”. In: *International Conference on Learning Representations (ICLR 2022)*.
- Bay, H., T. Tuytelaars, and L. Van Gool (2006). “Surf: Speeded up Robust Features”. In: *European Conference on Computer Vision*. Springer, pp. 404–417.
- Bludau, S., S. Eickhoff, H. Mohlberg, S. Caspers, A. Laird, P. Fox, A. Schleicher, K. Zilles, and K. Amunts (2014). “Cytoarchitecture, Probability Maps and Functions of the Human Frontal Pole”. In: *NeuroImage* 93 (Pt 2), pp. 260–275. DOI: 10.1016/j.neuroimage.2013.05.052.
- Bommasani, R. et al. (2022). *On the Opportunities and Risks of Foundation Models*. URL: <http://arxiv.org/abs/2108.07258> (visited on 10/24/2023). Pre-published.
- Brodmann, K. (1909). *Vergleichende Lokalisationslehre der Großhirnrinde*. Barth.
- Caliński, T. and J. and Harabasz (1974). “A Dendrite Method for Cluster Analysis”. In: *Communications in Statistics* 3.1, pp. 1–27. DOI: 10.1080/03610927408827101.
- Campbell, A. W. (1904). “Histological Studies on the Localisation of Cerebral Function”. In: *Journal of Mental Science* 50.211, pp. 651–662.
- Caron, M., I. Misra, J. Mairal, P. Goyal, P. Bojanowski, and A. Joulin (2020). “Unsupervised Learning of Visual Features by Contrasting Cluster Assignments”. In: *Advances in Neural Information Processing Systems*. Vol. 33, pp. 9912–9924.
- Casamitjana, A., M. Mancini, E. Robinson, L. Peter, R. Annunziata, J. Althonayan, S. Crampsie, E. Blackburn, B. Billot, A. Atzeni, O. Puonti, Y. Balbastre, P. Schmidt, J. Hughes, J. C.

- Augustinack, B. L. Edlow, L. Zöllei, D. L. Thomas, D. Kliemann, M. Bocchetta, C. Strand, J. L. Holton, Z. Jaunmuktane, and J. E. Iglesias (2025). “A Probabilistic Histological Atlas of the Human Brain for MRI Segmentation”. In: *Nature*, pp. 1–8. DOI: 10.1038/s41586-025-09708-2.
- Chan, T. and L. Vese (1999). “An Active Contour Model without Edges”. In: *Scale-Space Theories in Computer Vision*. Lecture Notes in Computer Science, pp. 141–151. DOI: 10.1007/3-540-48236-9_13.
- Chen, T., S. Kornblith, M. Norouzi, and G. Hinton (2020). “A Simple Framework for Contrastive Learning of Visual Representations”. In: *International Conference on Machine Learning (ICML 2020)*, pp. 1597–1607.
- Chen, X. and K. He (2021). “Exploring Simple Siamese Representation Learning”. In: *2021 IEEE/CVF Conference on Computer Vision and Pattern Recognition (CVPR)*, pp. 15750–15758.
- Chowdhery, A., S. Narang, J. Devlin, M. Bosma, G. Mishra, A. Roberts, P. Barham, H. W. Chung, C. Sutton, S. Gehrmann, P. Schuh, K. Shi, S. Tsvyashchenko, J. Maynez, A. Rao, P. Barnes, Y. Tay, N. Shazeer, V. Prabhakaran, E. Reif, N. Du, B. Hutchinson, R. Pope, J. Bradbury, J. Austin, M. Isard, G. Gur-Ari, P. Yin, T. Duke, A. Levskaya, S. Ghemawat, S. Dev, H. Michalewski, X. Garcia, V. Misra, K. Robinson, L. Fedus, D. Zhou, D. Ippolito, D. Luan, H. Lim, B. Zoph, A. Spiridonov, R. Sepassi, D. Dohan, S. Agrawal, M. Omernick, A. M. Dai, T. S. Pillai, M. Pellat, A. Lewkowycz, E. Moreira, R. Child, O. Polozov, K. Lee, Z. Zhou, X. Wang, B. Saeta, M. Diaz, O. Firat, M. Catasta, J. Wei, K. Meier-Hellstern, D. Eck, J. Dean, S. Petrov, and N. Fiedel (2023). “PaLM: Scaling Language Modeling with Pathways”. In: *J. Mach. Learn. Res.* 24.1, 240:11324–240:11436.
- Cignoni, P., M. Callieri, M. Corsini, M. Dellepiane, F. Ganovelli, and G. Ranzuglia (2008). “MeshLab: An Open-Source Mesh Processing Tool”. In: *Eurographics Italian Chapter Conference*. The Eurographics Association.
- Dadi, K., G. Varoquaux, A. Machlouzariides-Shalit, K. J. Gorgolewski, D. Wassermann, B. Thirion, and A. Mensch (2020). “Fine-Grain Atlases of Functional Modes for fMRI Analysis”. In: *NeuroImage* 221, p. 117126. DOI: 10.1016/j.neuroimage.2020.117126.
- Dickscheid, T., S. Bludau, C. Paquola, C. Schiffer, E. Upschulte, and K. Amunts (2021). *Layer-Specific Distributions of Segmented Cells in Different Cytoarchitectonic Regions of BigBrain Iso Cortex*. URL: <https://search.kg.ebrains.eu/instances/f06a2fd1-a9ca-42a3-b754-adaa025adb10>.
- Dickscheid, T., X. Gui, A. Simsek, C. Schiffer, J.-F. Mangin, Y. Leprince, V. Jirsa, J. G. Bjaalie, T. B. Leergaard, S. Bludau, and K. Amunts (2025). *Siiibra: A Software Tool Suite for Realizing a Multilevel Human Brain Atlas from Complex Data Resources*. DOI: 10.1101/2025.05.20.655042. URL: <https://www.biorxiv.org/content/10.1101/2025.05.20.655042v1> (visited on 06/24/2025). Pre-published.
- Dickscheid, T., S. Haas, S. Bludau, P. Glock, M. Huysegoms, and K. Amunts (2019). “Towards 3D Reconstruction of Neuronal Cell Distributions from Histological Human Brain Sections”. In: *Future Trends of HPC in a Disruptive Scenario* 34, p. 223.
- Ding, S.-L., J. J. Royall, S. M. Sunkin, L. Ng, B. A. C. Facer, P. Lesnar, A. Guillozet-Bongaarts, B. McMurray, A. Szafer, T. A. Dolbeare, A. Stevens, L. Tirrell, T. Benner, S. Caldejon, R. A. Dalley, N. Dee, C. Lau, J. Nyhus, M. Reding, Z. L. Riley, D. Sandman, E. Shen, A. van der Kouwe, A. Varjabedian, M. Write, L. Zollei, C. Dang, J. A. Knowles, C. Koch, J. W. Phillips, N. Sestan, P. Wohnoutka, H. R. Zielke, J. G. Hohmann, A. R. Jones, A. Bernard, M. J. Hawrylycz, P. R. Hof, B. Fischl, and E. S. Lein (2016). “Comprehensive Cellular-

- Resolution Atlas of the Adult Human Brain”. In: *Journal of Comparative Neurology* 524.16, pp. 3127–3481. DOI: [10.1002/cne.24080](https://doi.org/10.1002/cne.24080).
- Dong, Z., R. Li, Y. Wu, T. T. Nguyen, J. Chong, F. Ji, N. Tong, C. Chen, and J. H. Zhou (2024). “Brain-Jepa: Brain Dynamics Foundation Model with Gradient Positioning and Spatiotemporal Masking”. In: *Advances in Neural Information Processing Systems* 37, pp. 86048–86073.
- Dosovitskiy, A., L. Beyer, A. Kolesnikov, D. Weissenborn, X. Zhai, T. Unterthiner, M. Dehghani, M. Minderer, G. Heigold, S. Gelly, et al. (2020). “An Image Is Worth 16x16 Words: Transformers for Image Recognition at Scale”. In: *International Conference on Learning Representations (ICLR 2020)*.
- Fischler, M. A. and R. C. Bolles (1981). “Random Sample Consensus: A Paradigm for Model Fitting with Applications to Image Analysis and Automated Cartography”. In: *Communications of the ACM* 24.6, pp. 381–395.
- Fonov, V., A. C. Evans, K. Botteron, C. R. Almli, R. C. McKinstry, and D. L. Collins (2011). “Unbiased Average Age-Appropriate Atlases for Pediatric Studies”. In: *NeuroImage* 54.1, pp. 313–327. DOI: [10.1016/j.neuroimage.2010.07.033](https://doi.org/10.1016/j.neuroimage.2010.07.033).
- Geirhos, R., J.-H. Jacobsen, C. Michaelis, R. Zemel, W. Brendel, M. Bethge, and F. A. Wichmann (2020). “Shortcut Learning in Deep Neural Networks”. In: *Nature Machine Intelligence* 2.11, pp. 665–673. DOI: [10.1038/s42256-020-00257-z](https://doi.org/10.1038/s42256-020-00257-z).
- Geyer, S., A. Ledberg, A. Schleicher, S. Kinomura, T. Schormann, U. Bürgel, T. Klingberg, J. Larsson, K. Zilles, and P. E. Roland (1996). “Two Different Areas within the Primary Motor Cortex of Man”. In: *Nature* 382.6594 (6594), pp. 805–807. DOI: [10.1038/382805a0](https://doi.org/10.1038/382805a0).
- Geyer, S., A. Schleicher, and K. Zilles (1999). “Areas 3a, 3b, and 1 of Human Primary Somatosensory Cortex: 1. Microstructural Organization and Interindividual Variability”. In: *NeuroImage* 10.1, pp. 63–83. DOI: [10.1006/nimg.1999.0440](https://doi.org/10.1006/nimg.1999.0440).
- Glasser, M. F., T. S. Coalson, E. C. Robinson, C. D. Hacker, J. Harwell, E. Yacoub, K. Ugurbil, J. Andersson, C. F. Beckmann, and M. Jenkinson (2016). “A Multi-Modal Parcellation of Human Cerebral Cortex”. In: *Nature* 536.7615, pp. 171–178.
- Grill, J.-B., F. Strub, F. Altché, C. Tallec, P. H. Richemond, E. Buchatskaya, C. Doersch, B. A. Pires, Z. D. Guo, M. G. Azar, B. Piot, K. Kavukcuoglu, R. Munos, and M. Valko (2020). “Bootstrap Your Own Latent: A New Approach to Self-Supervised Learning”. In: *34th Conference on Neural Information Processing Systems (NeurIPS 2020)*.
- Haug, H. (1956). “Remarks on the Determination and Significance of the Gray Cell Coefficient”. In: *The Journal of Comparative Neurology* 104.3, pp. 473–492. DOI: [10.1002/cne.901040306](https://doi.org/10.1002/cne.901040306).
- He, K., H. Fan, Y. Wu, S. Xie, and R. Girshick (2020). “Momentum Contrast for Unsupervised Visual Representation Learning”. In: *2020 IEEE/CVF Conference on Computer Vision and Pattern Recognition (CVPR)*, pp. 9729–9738.
- He, K., X. Zhang, S. Ren, and J. Sun (2016). “Deep Residual Learning for Image Recognition”. In: *2016 IEEE Conference on Computer Vision and Pattern Recognition (CVPR)*, pp. 770–778.
- Hilgetag, C. C. and K. Amunts (2016). “Connectivity and Cortical Architecture”. In: *e-Neuroforum* 7.3, pp. 56–63. DOI: [10.1007/s13295-016-0028-0](https://doi.org/10.1007/s13295-016-0028-0).
- Hilgetag, C. C., S. F. Beul, S. J. van Albada, and A. Goulas (2019). “An Architectonic Type Principle Integrates Macroscopic Cortico-Cortical Connections with Intrinsic Cortical Circuits of the Primate Brain”. In: *Network neuroscience* 3.4, pp. 905–923.

- Holmes, C. J., R. Hoge, L. Collins, R. Woods, A. W. Toga, and A. C. Evans (1998). “Enhancement of MR Images Using Registration for Signal Averaging”. In: *Journal of Computer Assisted Tomography* 22.2, pp. 324–333.
- Ioffe, S. and C. Szegedy (2015). “Batch Normalization: Accelerating Deep Network Training by Reducing Internal Covariate Shift”. In: *International Conference on Machine Learning*, pp. 448–456.
- Jumper, J., R. Evans, A. Pritzel, T. Green, M. Figurnov, O. Ronneberger, K. Tunyasuvunakool, R. Bates, A. Žídek, A. Potapenko, A. Bridgland, C. Meyer, S. A. A. Kohl, A. J. Ballard, A. Cowie, B. Romera-Paredes, S. Nikolov, R. Jain, J. Adler, T. Back, S. Petersen, D. Reiman, E. Clancy, M. Zielinski, M. Steinegger, M. Pacholska, T. Berghammer, S. Bodenstein, D. Silver, O. Vinyals, A. W. Senior, K. Kavukcuoglu, P. Kohli, and D. Hassabis (2021). “Highly Accurate Protein Structure Prediction with AlphaFold”. In: *Nature* 596.7873 (7873), pp. 583–589. DOI: 10.1038/s41586-021-03819-2.
- Kazhdan, M., M. Bolitho, and H. Hoppe (2006). “Poisson Surface Reconstruction”. In: *Fourth Eurographics Symposium on Geometry Processing*. SGP ’06, pp. 61–70.
- Khosla, P., P. Teterwak, C. Wang, A. Sarna, Y. Tian, P. Isola, A. Maschinot, C. Liu, and D. Krishnan (2020). “Supervised Contrastive Learning”. In: *Advances in Neural Information Processing Systems*. Vol. 33. Curran Associates, Inc., pp. 18661–18673.
- Kikinis, R., S. D. Pieper, and K. G. Vosburgh (2014). “3D Slicer: A Platform for Subject-Specific Image Analysis, Visualization, and Clinical Support”. In: *Intraoperative Imaging and Image-Guided Therapy*. New York, NY: Springer, pp. 277–289. DOI: 10.1007/978-1-4614-7657-3_19. URL: 10.1007/978-1-4614-7657-3_19.
- Kügelgen, J. V., Y. Sharma, L. Gresele, W. Brendel, B. Schölkopf, M. Besserve, and F. Locatello (2021). “Self-Supervised Learning with Data Augmentations Provably Isolates Content from Style”. In: *Advances in Neural Information Processing Systems*.
- Leprince, Y., F. Poupon, T. Delzescaux, D. Hasboun, C. Poupon, and D. Rivière (2015). “Combined Laplacian-equivolumic Model for Studying Cortical Lamination with Ultra High Field MRI (7 T)”. In: *2015 IEEE 18th International Symposium on Biomedical Imaging (ISBI 2015)*, pp. 580–583. DOI: 10.1109/ISBI.2015.7163940.
- Lewiner, T., H. Lopes, A. W. Vieira, and G. Tavares (2003). “Efficient Implementation of Marching Cubes’ Cases with Topological Guarantees”. In: *Journal of Graphics Tools* 8.2, pp. 1–15. DOI: 10.1080/10867651.2003.10487582.
- Lewis, L., C. Lepage, M. Fournier, K. Zilles, K. Amunts, and A. Evans (2014). “BigBrain: Initial Tissue Classification and Surface Extraction”. In: *Annual Meeting of the Organization for Human Brain Mapping*.
- Margulies, D. S., S. S. Ghosh, A. Goulas, M. Falkiewicz, J. M. Huntenburg, G. Langs, G. Bezgin, S. B. Eickhoff, F. X. Castellanos, M. Petrides, E. Jefferies, and J. Smallwood (2016). “Situating the Default-Mode Network along a Principal Gradient of Macroscale Cortical Organization”. In: *Proceedings of the National Academy of Sciences* 113.44, pp. 12574–12579. DOI: 10.1073/pnas.1608282113.
- Markello, R. D., J. Y. Hansen, Z.-Q. Liu, V. Bazinet, G. Shafiei, L. E. Suárez, N. Blostein, J. Seidlitz, S. Baillet, T. D. Satterthwaite, M. M. Chakravarty, A. Raznahan, and B. Misic (2022). “Neuromaps: Structural and Functional Interpretation of Brain Maps”. In: *Nature Methods* 19.11 (11), pp. 1472–1479. DOI: 10.1038/s41592-022-01625-w.
- Márquez-Neila, P., L. Baumela, and L. Alvarez (2014). “A Morphological Approach to Curvature-Based Evolution of Curves and Surfaces”. In: *IEEE Transactions on Pattern Analysis and Machine Intelligence* 36.1, pp. 2–17. DOI: 10.1109/TPAMI.2013.106.

- Mathis, M. W., A. P. Rotondo, E. F. Chang, A. S. Tolia, and A. Mathis (2024). “Decoding the Brain: From Neural Representations to Mechanistic Models”. In: *Cell* 187.21, pp. 5814–5832.
- McInnes, L., J. Healy, N. Saul, and L. Großberger (2018). “UMAP: Uniform Manifold Approximation and Projection”. In: *Journal of Open Source Software* 3.29, p. 861. DOI: 10.21105/joss.00861.
- Merker, B. (1983). “Silver Staining of Cell Bodies by Means of Physical Development”. In: *Journal of Neuroscience Methods* 9.3, pp. 235–241. DOI: 10.1016/0165-0270(83)90086-9.
- Mesulam, M. M. (1998). “From Sensation to Cognition.” In: *Brain* 121.6, pp. 1013–1052. DOI: 10.1093/brain/121.6.1013.
- Ngnawé, J., S. Sahoo, Y. Pequignot, F. Precioso, and C. Gagné (2024). *Detecting Brittle Decisions for Free: Leveraging Margin Consistency in Deep Robust Classifiers*. DOI: 10.48550/arXiv.2406.18451. URL: <http://arxiv.org/abs/2406.18451> (visited on 02/07/2025). Pre-published.
- Oord, A. van den, Y. Li, and O. Vinyals (2019). “Representation Learning with Contrastive Predictive Coding”. URL: <http://arxiv.org/abs/1807.03748> (visited on 12/10/2020).
- OpenAI et al. (2024). *GPT-4 Technical Report*. DOI: 10.48550/arXiv.2303.08774. URL: <http://arxiv.org/abs/2303.08774> (visited on 08/18/2025). Pre-published.
- Oquab, M., T. Darcet, T. Moutakanni, H. Vo, M. Szafraniec, V. Khalidov, P. Fernandez, D. Haziza, F. Massa, A. El-Nouby, M. Assran, N. Ballas, W. Galuba, R. Howes, P.-Y. Huang, S.-W. Li, I. Misra, M. Rabbat, V. Sharma, G. Synnaeve, H. Xu, H. Jegou, J. Mairal, P. Labatut, A. Joulin, and P. Bojanowski (2024). *DINOv2: Learning Robust Visual Features without Supervision*. URL: <http://arxiv.org/abs/2304.07193>. Pre-published.
- Otsu, N. (1979). “A Threshold Selection Method from Gray-Level Histograms”. In: *IEEE Transactions on Systems, Man, and Cybernetics* 9.1, pp. 62–66. DOI: 10.1109/TSMC.1979.4310076.
- Paquola, C., J. Royer, L. B. Lewis, C. Lepage, T. Glatard, K. Wagstyl, J. DeKraaker, P.-J. Toussaint, S. L. Valk, L. Collins, A. R. Khan, K. Amunts, A. C. Evans, T. Dickscheid, and B. Bernhardt (2021). “The BigBrainWarp Toolbox for Integration of BigBrain 3D Histology with Multimodal Neuroimaging”. In: *eLife* 10, e70119. DOI: 10.7554/eLife.70119.
- Paquola, C., R. V. D. Wael, K. Wagstyl, R. A. I. Bethlehem, S.-J. Hong, J. Seidlitz, E. T. Bullmore, A. C. Evans, B. Misic, D. S. Margulies, J. Smallwood, and B. C. Bernhardt (2019). “Microstructural and Functional Gradients Are Increasingly Dissociated in Transmodal Cortices”. In: *PLOS Biology* 17.5, e3000284. DOI: 10.1371/journal.pbio.3000284.
- Paszke, A., S. Gross, F. Massa, A. Lerer, J. Bradbury, G. Chanan, T. Killeen, Z. Lin, N. Gimelshein, L. Antiga, A. Desmaison, A. Köpf, E. Yang, Z. DeVito, M. Raison, A. Tejani, S. Chilamkurthy, B. Steiner, L. Fang, J. Bai, and S. Chintala (2019). “PyTorch: An Imperative Style, High-Performance Deep Learning Library”. In: *33rd Conference on Neural Information Processing Systems (NeurIPS 2019)*.
- Pizer, S. M., E. P. Amburn, J. D. Austin, R. Cromartie, A. Geselowitz, T. Greer, B. ter Haar Romeny, J. B. Zimmerman, and K. Zuiderveld (1987). “Adaptive Histogram Equalization and Its Variations”. In: *Computer vision, graphics, and image processing* 39.3, pp. 355–368.
- Pohlen, T., A. Hermans, M. Mathias, and B. Leibe (2017). “Full-Resolution Residual Networks for Semantic Segmentation in Street Scenes”. In: *IEEE Conference on Computer Vision and Pattern Recognition (CVPR’17)*.
- Radford, A., J. W. Kim, C. Hallacy, A. Ramesh, G. Goh, S. Agarwal, G. Sastry, A. Askell, P. Mishkin, and J. Clark (2021). “Learning Transferable Visual Models from Natural Language Supervision”. In: *International Conference on Machine Learning*. PmLR, pp. 8748–8763.

- Rivière, D., D. Geffroy, I. Denghien, N. Souedet, and Y. Cointepas (2009). “BrainVISA: An Extensible Software Environment for Sharing Multimodal Neuroimaging Data and Processing Tools”. In: *NeuroImage* 47, S163. DOI: 10.1016/S1053-8119(09)71720-3.
- Royer, J., R. Rodríguez-Cruces, S. Tavakol, S. Larivière, P. Herholz, Q. Li, R. Vos de Wael, C. Paquola, O. Benkarim, B.-y. Park, A. J. Lowe, D. Margulies, J. Smallwood, A. Bernasconi, N. Bernasconi, B. Frauscher, and B. C. Bernhardt (2022). “An Open MRI Dataset For Multiscale Neuroscience”. In: *Scientific Data* 9.1, p. 569. DOI: 10.1038/s41597-022-01682-y.
- Schiffer, C., K. Amunts, S. Harmeling, and T. Dickscheid (2021a). “Contrastive Representation Learning For Whole Brain Cytoarchitectonic Mapping In Histological Human Brain Sections”. In: *2021 IEEE 18th International Symposium on Biomedical Imaging (ISBI 2021)*, pp. 603–606. DOI: 10.1109/ISBI48211.2021.9433986.
- Schiffer, C., S. Harmeling, K. Amunts, and T. Dickscheid (2021b). “2D Histology Meets 3D Topology: Cytoarchitectonic Brain Mapping with Graph Neural Networks”. In: *Medical Image Computing and Computer Assisted Intervention – MICCAI 2021*, pp. 395–404. DOI: 10.1007/978-3-030-87237-3_38.
- Schleicher, A., K. Amunts, S. Geyer, P. Morosan, and K. Zilles (1999). “Observer-Independent Method for Microstructural Parcellation of Cerebral Cortex: A Quantitative Approach to Cytoarchitectonics”. In: *NeuroImage* 9.1, pp. 165–177. DOI: 10.1006/nimg.1998.0385.
- Spitzer, H., K. Amunts, S. Harmeling, and T. Dickscheid (2018). “Compact Feature Representations for Human Brain Cytoarchitecture Using Self-Supervised Learning”. In: *Medical Imaging with Deep Learning (MIDL 2018)*.
- Surazhsky, V. and C. Gotsman (2003). “Explicit Surface Remeshing”. In: *Eurographics Symposium on Geometry Processing*.
- Tak, D., B. A. Garomsa, A. Zapaishchykova, T. L. Chaunzwa, J. C. Climent Pardo, Z. Ye, J. Zielke, Y. Ravipati, S. Pai, S. Vajapeyam, M. Mahootiha, M. Parker, L. R. G. Pike, C. Smith, A. M. Familiar, K. X. Liu, S. Prabhu, O. Arnaout, P. Bandopadhyay, A. Nabavizadeh, S. Mueller, H. J. Aerts, R. Y. Huang, T. Y. Poussaint, and B. H. Kann (2026). “A Generalizable Foundation Model for Analysis of Human Brain MRI”. In: *Nature Neuroscience*, pp. 1–12. DOI: 10.1038/s41593-026-02202-6.
- Thörnig, P. (2021). “JURECA: Data Centric and Booster Modules Implementing the Modular Supercomputing Architecture at Jülich Supercomputing Centre”. In: *Journal of large-scale research facilities JLSRF* 7, A182–A182. DOI: 10.17815/jlsrf-7-182.
- Tian, Y., C. Sun, B. Poole, D. Krishnan, C. Schmid, and P. Isola (2020). “What Makes for Good Views for Contrastive Learning?” In: *Advances in Neural Information Processing Systems* 33, pp. 6827–6839.
- Upschulte, E., S. Harmeling, K. Amunts, and T. Dickscheid (2022). “Contour Proposal Networks for Biomedical Instance Segmentation”. In: *Medical Image Analysis*. DOI: 10.1016/j.media.2022.102371.
- Van Essen, D. C., M. F. Glasser, D. L. Dierker, J. Harwell, and T. Coalson (2012). “Parcellations and Hemispheric Asymmetries of Human Cerebral Cortex Analyzed on Surface-Based Atlases”. In: *Cerebral Cortex* 22.10, pp. 2241–2262. DOI: 10.1093/cercor/bhr291.
- Vogt, C. and O. Vogt (1919). *Allgemeine Ergebnisse unserer Hirnforschung*. Vol. 21. JA Barth.
- Von Economo, C. (1925). *Die Cytoarchitektonik der Hirnrinde des erwachsenen Menschen*. Wien: Springer.
- Wagstyl, K., S. Larocque, G. Cucurull, C. Lepage, J. P. Cohen, S. Bludau, N. Palomero-Gallagher, L. B. Lewis, T. Funck, and H. Spitzer (2020). “BigBrain 3D Atlas of Cortical

- Layers: Cortical and Laminar Thickness Gradients Diverge in Sensory and Motor Cortices”. In: *PLOS Biology* 18.4, e3000678.
- Wagstyl, K., S. Larocque, G. Cucurull, C. Lepage, J. P. Cohen, S. Bludau, N. Palomero-Gallagher, L. B. Lewis, T. Funck, H. Spitzer, T. Dickscheid, P. C. Fletcher, A. Romero, K. Zilles, K. Amunts, Y. Bengio, and A. C. Evans (2022). *Cortical Intensity Profiles Sampled across BigBrain Isocortex (v1.0)*. EBRAINS. DOI: 10.25493/18ED-DS3. URL: <https://search.kg.ebrains.eu/instances/26d25994-634c-40af-b88f-2a36e8e1d508>.
- Wagstyl, K., C. Lepage, S. Bludau, K. Zilles, P. C. Fletcher, K. Amunts, and A. C. Evans (2018). “Mapping Cortical Laminar Structure in the 3d Bigbrain”. In: *Cerebral Cortex* 28.7, pp. 2551–2562.
- Yeo, B. T. T., F. M. Krienen, J. Sepulcre, M. R. Sabuncu, D. Lashkari, M. Hollinshead, J. L. Roffman, J. W. Smoller, L. Zöllei, J. R. Polimeni, B. Fischl, H. Liu, and R. L. Buckner (2011). “The Organization of the Human Cerebral Cortex Estimated by Intrinsic Functional Connectivity”. In: *Journal of Neurophysiology* 106.3, pp. 1125–1165. DOI: 10.1152/jn.00338.2011.
- You, Y., I. Gitman, and B. Ginsburg (2017). *Large Batch Training of Convolutional Networks*. DOI: 10.48550/arXiv.1708.03888. URL: <http://arxiv.org/abs/1708.03888> (visited on 10/16/2025). Pre-published.
- Zbontar, J., L. Jing, I. Misra, Y. LeCun, and S. Deny (2021). “Barlow Twins: Self-Supervised Learning via Redundancy Reduction”. In: *Proceedings of the 38th International Conference on Machine Learning*. International Conference on Machine Learning. PMLR, pp. 12310–12320.
- Zilles, K. and K. Amunts (2010). “Centenary of Brodmann’s Map—Conception and Fate”. In: *Nature Reviews Neuroscience* 11.2, pp. 139–145. DOI: 10.1038/nrn2776.
- (2013). “Individual Variability Is Not Noise”. In: *Trends in Cognitive Sciences* 17.4, pp. 153–155. DOI: 10.1016/j.tics.2013.02.003.

Table 2: List of 113 brain areas used for brain area classification. Areas are denoted by the nomenclature of the Julich Brain Atlas (Amunts et al., 2020), e.g., *hOc1* for *human occipital area 1* or *FG1* for *fusiform gyrus area 1*.

occipital lobe							
hOc1	hOc2	hOc3v	hOc4v	hOc3d	hOc4d	hOc4la	hOc4lp
hOc5	hOc6						
parietal lobe							
Ip1	Ip2	Ip3	Ip4	1	2	3a	3b
5L	5M	5Ci	7PC	7A	hIP3	PF	PFcm
PFm	PFop	PFFt	PGa	PGp	hIP1	hIP2	hIP4
hIP5	hIP6	hIP7	hIP8	hPO1			
temporal lobe							
FG1	FG2	FG3	FG4	Te 1.0	Te 1.1	Te 1.2	Te 2.1
Te 2.2	Te 3	STS1	STS2	TeI	TI		
insula							
Ig1	Ig2	Id1	Ig3	Id2	Id3	Id4	Id5
Id6	Ia7	Ia1					
frontal lobe							
4a	4p	6d1	6d2	6d3	6v1	6v2	6r1
6mp	6ma	11a	11p	13	Fo4	Fo5	Fo6
Fo7	IFJ1	IFJ2	IFS1	IFS2	IFS3	IFS4	8a
8b	8c	8d	SFS1	SFS2	FMS1	MFG1	44
45	Op5	Op6	Op7	Op8	Op9		
limbic lobe							
25a	25p	s24a	s24b	s32	p24a	p24b	pv24c
pd24cd	pd24cv	p32					

11 Supplementary material

11.1 List of cytoarchitectonic areas

Table 3 shows the list of areas from the Julich Brain Atlas (version 3.1, Amunts et al. (2020)) used for analyses presented in Figure 2. Table 2 provides the names for the 113 areas used in cytoarchitectonic classification, selected as the subset of atlas annotations available in at least four of the ten brains analyzed in this study.

11.2 Extended embedding analysis

Following common practice in self-supervised learning (Chen et al., 2020), CytoNet was trained with a shallow projection head appended to the backbone. We compared the latent space structure of features extracted from the backbone (our default), and after the shallow projection head of CytoNet-ViT (1M). Backbone features preserved brain identity (Figure 7A,C,E), whereas projected features showed minimal brain separation and instead aligned strongly with hemisphere (CHI 11577.88 \rightarrow 28416.23) and atlas label (CHI 709.04 \rightarrow 3648.73). Thus, the projection layers effectively suppressed brain-specific artifacts (e.g., staining, morphology, sectioning) and emphasized spatially consistent cytoarchitectonic organization. In the held-out brain, projections retained a global anterior–posterior structure but showed weaker differentiation by atlas

Table 3: List of areas from the Julich Brain Atlas (version 3.1, Amunts et al. (2020)) used in Figure 2. For brevity, pre- and postfixes to the area name are omitted (e.g., “Area hOc1 (V1, 17, CalcS)” is abbreviated as “hOc1”). Indices of areas in the similarity matrices in Figure 2 are provided.

occipital lobe							
0	hOc1	3	hOc3v	6	hOc4lp	9	hOc6
1	hOc2	4	hOc4d	7	hOc4v		
2	hOc3d	5	hOc4la	8	hOc5		
parietal lobe							
10	1	18	7M	26	PFcm	34	hIP3
11	2	19	7P	27	PFm	35	hIP4
12	3a	20	7PC	28	PFop	36	hIP5
13	3b	21	Op1	29	PFt	37	hIP6
14	5Ci	22	Op2	30	PGa	38	hIP7
15	5L	23	Op3	31	PGp	39	hIP8
16	5M	24	Op4	32	hIP1	40	hPO1
17	7A	25	PF	33	hIP2		
temporal lobe							
41	CoS1	47	OTS1	53	TI	59	Te 2.2
42	FG1	48	Ph1	54	TPJ	60	Te 3
43	FG2	49	Ph2	55	Te 1.0	61	TeI
44	FG3	50	Ph3	56	Te 1.1		
45	FG4	51	STS1	57	Te 1.2		
46	FG5	52	STS2	58	Te 2.1		
insula							
62	Ia1	66	Id10	70	Id5	74	Id9
63	Ia2	67	Id2	71	Id6	75	Ig1
64	Ia3	68	Id3	72	Id7	76	Ig2
65	Id1	69	Id4	73	Id8	77	Ig3
frontal lobe							
78	44	90	6v3	102	Fp1	114	Op10
79	45	91	8d1	103	Fp2	115	Op5
80	4a	92	8d2	104	IFJ1	116	Op6
81	4p	93	8v1	105	IFJ2	117	Op7
82	6d1	94	8v2	106	IFS1	118	Op8
83	6d2	95	Fo1	107	IFS2	119	Op9
84	6d3	96	Fo2	108	IFS3	120	SFG2
85	6ma	97	Fo3	109	IFS4	121	SFG3
86	6mp	98	Fo4	110	MFG1	122	SFG4
87	6r1	99	Fo5	111	MFG2	123	SFS1
88	6v1	100	Fo6	112	MFG4	124	SFS2
89	6v2	101	Fo7	113	MFG5		
limbic lobe							
125	33	128	s32	131	CA3	134	TrS
126	EC	129	CA1	132	DG	135	Tu
127	p32	130	CA2	133	HATA	136	TuTi

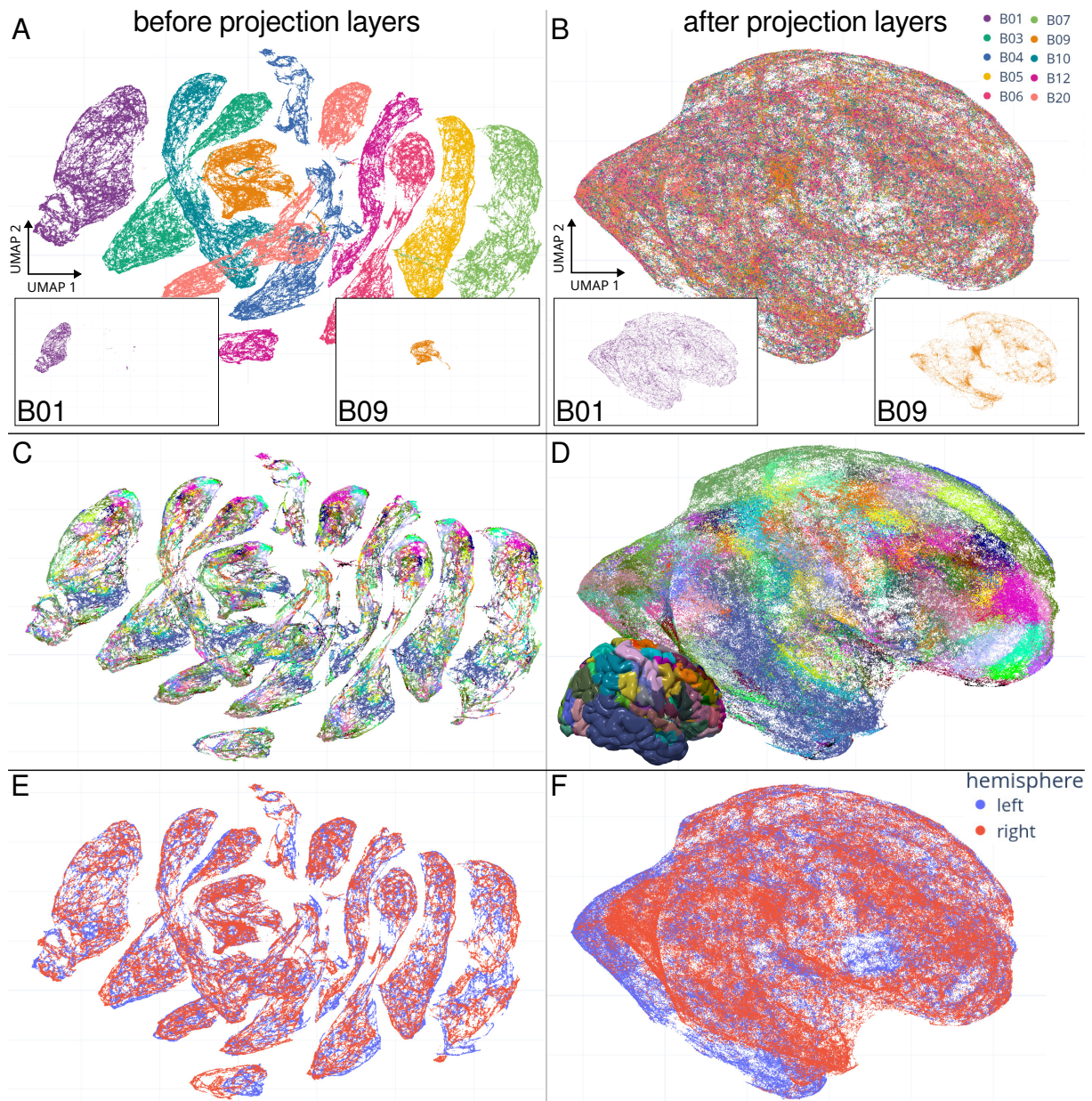


Figure 7: 2D UMAP embeddings from features before (left) and after (right) the projection layers of CytoNet-ViT (1M). Embeddings are color coded by brain (A, B), Julich Brain labels (C, D), and hemisphere (E, F). Features extracted before the projection layers form brain-specific clusters in the UMAP space (A) with similar internal arrangement of atlas labels (C) and hemispheres (E). In comparison, features extracted after the projection layers show strong alignment between points from different brains (B) with consistent atlas labels (D) and hemispheres (F). The transfer brain B09 appears more compact and less differentiated than other brains, both before (A) and after the projection (B).

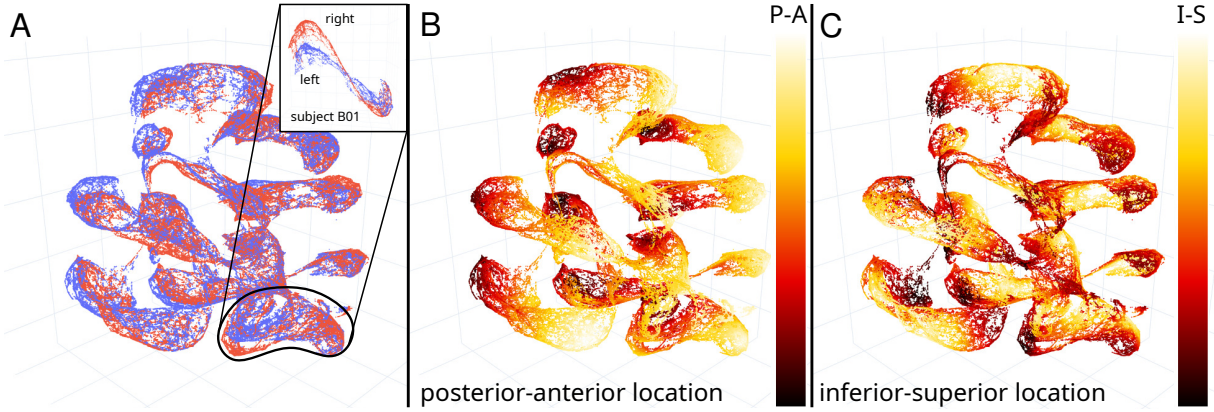


Figure 8: 3D UMAP plots of CytoNet-ViT (1M) features, colored by hemisphere (A), posterior-anterior location (B) and inferior-superior location (C) in the MNI Colin 27 space. Embedding dimensions strongly correlated with spatial locations, forming distinct hemisphere-specific manifolds.

label (CHI 77.63 vs. 122.96 ± 12.17) and hemisphere (CHI 27.85 vs. 1633.94 ± 231.41), reflecting reduced feature specificity.

Complementing our 2D UMAP analyses (Figure 2), we visualized 3D UMAP embeddings colored by hemisphere, anterior-posterior and inferior-superior axes (Figure 8). The results show strong alignment between embedding locations and spatial locations, including distinct hemisphere-specific manifolds.

11.3 Cross-brain prediction of spatial coordinates

To assess how well CytoNet features generalize across brains in terms of spatial encoding, linear regression models were trained to predict MNI coordinates from feature representations. Specifically, one model was fitted per spatial axis (anterior-posterior, inferior-superior, and left-right) using features extracted from brain B20. Models were trained using 5-fold cross-validation on B20, and then applied to predict spatial coordinates in other brains based on their CytoNet-ViT-B (1M) features. Euclidean prediction errors were computed in MNI Colin 27 reference space (Table 4), where the postmortem brains are being presented after registration (Amunts et al., 2020). This approach allows evaluating how consistently CytoNet encodes spatial location across different individuals. Prediction errors were approximately 10 mm in anterior-posterior and inferior-superior directions. Errors in left-right direction were larger (approximately 20 mm), likely due to structural left-right symmetries. Substantially higher errors were observed in the unseen brain B09, indicating reduced spatial generalization without brain-specific pretraining. Such cross-brain prediction experiments can serve as a proxy for evaluating the general utility of learned features for other structural properties, such as cortical thickness, layer boundaries, or cell density, which are often spatially organized and may benefit from similarly aligned representations.

11.4 Extended scores for brain area classification and layer segmentation

Table 5 shows macro-F1 scores, top-1 and top-3 accuracy achieved by different models in brain area classification (Section 4.5) on seen, transfer, and unseen subjects. Performance for finetuning (trainable encoder) and linear probing (frozen encoder) are reported.

Table 4: Euclidean distance between true and predicted locations in MNI Colin 27 space. Linear models were fitted on CytoNet-ViT (1M) features from B20 and applied to features from other brains. Mean and standard deviation across 5-fold cross validation on B20 are shown. Prediction errors in anterior-posterior and inferior-superior directions were approximately 10 mm, and approximately 20 mm in left-right direction. Prediction errors in the unseen brain B09 were significantly higher than brains that were included for pretraining of CytoNet-ViT (1M).

dimension	left-right	anterior-posterior	inferior-superior
B01	19.62 ± 0.12	11.56 ± 0.11	9.89 ± 0.12
B03	19.08 ± 0.08	11.97 ± 0.15	10.92 ± 0.10
B04	18.60 ± 0.09	12.19 ± 0.12	9.98 ± 0.04
B05	20.10 ± 0.29	12.87 ± 0.08	9.79 ± 0.09
B06	18.01 ± 0.43	12.97 ± 0.06	9.79 ± 0.05
B07	21.16 ± 0.13	15.91 ± 0.18	12.04 ± 0.26
B09	42.67 ± 0.35	22.42 ± 0.08	16.19 ± 0.11
B10	20.09 ± 0.16	12.93 ± 0.17	9.73 ± 0.03
B12	19.08 ± 0.26	10.80 ± 0.04	9.65 ± 0.10

CytoNet-ViT (1M) P was trained for area classification on the output of the projection layer rather than the backbone. Using linear probing, its classification performance dropped markedly compared to models using the backbone features, indicating that the projection layer discards or reshapes information essential for brain area classification. After finetuning, the model matched or exceeded the original backbone-based performance, especially on transfer and unseen subjects. These improvements, however, likely reflect the additional model capacity rather than the intrinsic utility of the pretrained projection space, making its specific contribution difficult to isolate.

CytoNet-ViT (1M) M was pretrained using coordinates from the ICBM 152 template (ICBM 2009c Nonlinear asymmetric, Fonov et al. (2011)) instead of MNI Colin 27. MNI Colin 27 was chosen as default because it provides a single-subject template with well-defined cortical landmarks, whereas ICBM 152 offers a population average with better inter-subject correspondence. Coordinates were non-linearly transformed from MNI Colin 27 to ICBM 152 space using siibra-python (Dickscheid et al., 2025). The pretrained model was then linearly probed and finetuned for brain area classification. Pretraining on ICBM 152 yielded classification scores slightly below those obtained with Colin27, but overall performance was comparable, suggesting that the choice of template has limited impact on the learned representations. Notably, transforming MNI Colin 27 coordinates to ICBM MNI 152 rather than natively aligning sections to ICBM MNI 152 may introduce additional errors. The observed differences likely reflect residual registration errors in the range of a few hundred micrometers, which are small compared to the millimeter-scale distances used in the loss but may still introduce local misalignments that affect pretraining. Natively aligning histological sections to ICBM 152 would allow a more direct assessment of template choice, but is challenging due to the limited availability of well-defined landmarks for registration.

We evaluated the impact of the selected transfer brain by linear probing of CytoNet-ViT (1M) with training data from different sets of brains (Table 6), keeping the unseen brain B09

Table 5: Scores for brain area classification obtained by different models using linear evaluation and finetuning. Mean and standard deviation of scores across three training runs with different random initialization are reported. The model suffixed with *P* was trained on outputs of the projection layer used during contrastive learning rather than backbone features. The model suffixed with *M* was pretrained using spatial coordinates from the ICBM 152 space rather than MNI Colin 27 reference template.

seen brains	linear probing (encoder frozen)			finetuning (encoder trainable)		
	macro-F1	top-1 acc	top-3 acc	macro-F1	top-1 acc	top-3 acc
scratch	-	-	-	0.39 ± 0.33	0.45 ± 0.32	0.64 ± 0.43
scratch-ViT	-	-	-	0.60 ± 0.01	0.65 ± 0.01	0.87 ± 0.01
SimCLR (200k)	0.24 ± 0.00	0.33 ± 0.00	0.55 ± 0.00	0.33 ± 0.28	0.36 ± 0.31	0.55 ± 0.46
SimCLR (1M)	0.15 ± 0.01	0.25 ± 0.01	0.43 ± 0.01	0.44 ± 0.01	0.51 ± 0.01	0.78 ± 0.02
SimCLR-ViT (200k)	0.06 ± 0.00	0.17 ± 0.01	0.30 ± 0.01	0.33 ± 0.09	0.39 ± 0.09	0.67 ± 0.10
SimCLR-ViT (1M)	0.05 ± 0.00	0.16 ± 0.01	0.29 ± 0.01	0.37 ± 0.06	0.45 ± 0.06	0.72 ± 0.06
SupCon	0.61 ± 0.00	0.66 ± 0.00	0.91 ± 0.00	0.59 ± 0.01	0.65 ± 0.01	0.89 ± 0.01
SupCon-ViT	0.60 ± 0.00	0.65 ± 0.00	0.91 ± 0.00	0.51 ± 0.08	0.57 ± 0.08	0.84 ± 0.07
CytoNet (200k)	0.64 ± 0.00	0.69 ± 0.00	0.93 ± 0.00	0.64 ± 0.01	0.69 ± 0.01	0.92 ± 0.01
CytoNet (1M)	0.54 ± 0.00	0.62 ± 0.00	0.90 ± 0.00	0.67 ± 0.02	0.72 ± 0.01	0.94 ± 0.01
CytoNet-ViT (200k)	0.54 ± 0.01	0.61 ± 0.01	0.90 ± 0.01	0.67 ± 0.00	0.72 ± 0.00	0.94 ± 0.00
CytoNet-ViT (1M)	0.69 ± 0.00	0.74 ± 0.00	0.96 ± 0.00	0.71 ± 0.02	0.76 ± 0.01	0.95 ± 0.01
CytoNet-ViT (1M) P	0.38 ± 0.00	0.44 ± 0.00	0.79 ± 0.00	0.71 ± 0.00	0.75 ± 0.00	0.94 ± 0.00
CytoNet-ViT (1M) M	0.54 ± 0.00	0.60 ± 0.00	0.90 ± 0.00	0.65 ± 0.05	0.70 ± 0.04	0.93 ± 0.02
transfer brain						
scratch	-	-	-	0.10 ± 0.08	0.19 ± 0.16	0.34 ± 0.26
scratch-ViT	-	-	-	0.15 ± 0.02	0.27 ± 0.03	0.49 ± 0.04
SimCLR (200k)	0.10 ± 0.00	0.21 ± 0.01	0.39 ± 0.01	0.11 ± 0.10	0.21 ± 0.17	0.38 ± 0.30
SimCLR (1M)	0.08 ± 0.00	0.20 ± 0.01	0.35 ± 0.01	0.14 ± 0.00	0.25 ± 0.02	0.47 ± 0.04
SimCLR-ViT (200k)	0.05 ± 0.00	0.16 ± 0.01	0.26 ± 0.01	0.14 ± 0.04	0.24 ± 0.05	0.48 ± 0.07
SimCLR-ViT (1M)	0.05 ± 0.00	0.17 ± 0.01	0.27 ± 0.01	0.13 ± 0.04	0.24 ± 0.09	0.46 ± 0.11
SupCon	0.22 ± 0.00	0.38 ± 0.00	0.67 ± 0.00	0.17 ± 0.02	0.30 ± 0.02	0.55 ± 0.03
SupCon-ViT	0.25 ± 0.00	0.41 ± 0.00	0.69 ± 0.00	0.15 ± 0.02	0.28 ± 0.04	0.52 ± 0.06
CytoNet (200k)	0.32 ± 0.00	0.49 ± 0.00	0.79 ± 0.00	0.18 ± 0.02	0.33 ± 0.02	0.58 ± 0.05
CytoNet (1M)	0.35 ± 0.00	0.52 ± 0.00	0.84 ± 0.00	0.17 ± 0.00	0.33 ± 0.02	0.56 ± 0.02
CytoNet-ViT (200k)	0.32 ± 0.01	0.49 ± 0.01	0.82 ± 0.02	0.30 ± 0.01	0.46 ± 0.00	0.77 ± 0.01
CytoNet-ViT (1M)	0.38 ± 0.00	0.56 ± 0.00	0.88 ± 0.00	0.26 ± 0.03	0.43 ± 0.03	0.71 ± 0.04
CytoNet-ViT (1M) P	0.23 ± 0.00	0.36 ± 0.00	0.71 ± 0.00	0.30 ± 0.01	0.48 ± 0.01	0.76 ± 0.01
CytoNet-ViT (1M) M	0.37 ± 0.00	0.53 ± 0.00	0.87 ± 0.00	0.20 ± 0.02	0.36 ± 0.03	0.62 ± 0.03
unseen brain						
scratch	-	-	-	0.12 ± 0.09	0.24 ± 0.14	0.41 ± 0.23
scratch-ViT	-	-	-	0.14 ± 0.00	0.28 ± 0.00	0.47 ± 0.01
SimCLR (200k)	0.10 ± 0.00	0.20 ± 0.00	0.36 ± 0.01	0.13 ± 0.11	0.22 ± 0.18	0.39 ± 0.32
SimCLR (1M)	0.08 ± 0.00	0.17 ± 0.01	0.32 ± 0.01	0.16 ± 0.02	0.28 ± 0.02	0.51 ± 0.03
SimCLR-ViT (200k)	0.03 ± 0.00	0.12 ± 0.00	0.21 ± 0.01	0.11 ± 0.01	0.21 ± 0.04	0.42 ± 0.04
SimCLR-ViT (1M)	0.04 ± 0.00	0.13 ± 0.00	0.23 ± 0.01	0.12 ± 0.03	0.24 ± 0.04	0.45 ± 0.07
SupCon	0.23 ± 0.00	0.36 ± 0.01	0.62 ± 0.00	0.18 ± 0.01	0.32 ± 0.01	0.54 ± 0.01
SupCon-ViT	0.24 ± 0.00	0.38 ± 0.00	0.64 ± 0.01	0.14 ± 0.04	0.27 ± 0.06	0.49 ± 0.09
CytoNet (200k)	0.28 ± 0.00	0.43 ± 0.00	0.73 ± 0.01	0.16 ± 0.01	0.31 ± 0.02	0.52 ± 0.02
CytoNet (1M)	0.25 ± 0.00	0.37 ± 0.00	0.66 ± 0.01	0.17 ± 0.03	0.32 ± 0.04	0.52 ± 0.05
CytoNet-ViT (200k)	0.24 ± 0.01	0.37 ± 0.01	0.67 ± 0.01	0.23 ± 0.01	0.37 ± 0.00	0.64 ± 0.01
CytoNet-ViT (1M)	0.24 ± 0.00	0.36 ± 0.00	0.64 ± 0.00	0.19 ± 0.02	0.35 ± 0.02	0.57 ± 0.03
CytoNet-ViT (1M) P	0.18 ± 0.00	0.27 ± 0.00	0.55 ± 0.00	0.20 ± 0.01	0.36 ± 0.01	0.59 ± 0.02
CytoNet-ViT (1M) M	0.23 ± 0.00	0.36 ± 0.00	0.65 ± 0.00	0.16 ± 0.01	0.29 ± 0.03	0.53 ± 0.03

Table 6: Scores for brain area classification obtained by linear probing of CytoNet-ViT (1M) backbone with cross-validation across transfer brains. Models were pre-trained in different training settings, each considering one of the brains B01, B03, B04, B05, B06, B07, B10, B12, and B20 as transfer brain, and the remaining as seen brains. In all cases, B09 was considered as unseen brain. Performance on seen brains and the unseen is largely independent of the brain used for pretraining. Performance on the respective transfer brain varies slightly, which is likely a result of different subsets of areas that were annotated in each brain.

	macro-F1	top-1 acc	top-3 acc
seen brains	0.70 ± 0.00	0.74 ± 0.00	0.96 ± 0.00
transfer brain	0.37 ± 0.08	0.57 ± 0.02	0.88 ± 0.01
unseen brain	0.23 ± 0.00	0.36 ± 0.00	0.64 ± 0.00

Table 7: Macro-F1 scores for cortical layer segmentation across different models and training fractions. Mean and standard deviation are reported over 5-fold cross-validation for each model, using either linear probing or finetuning. Models were trained on increasing fractions of the training set, and evaluated on a dedicated test set comprising 184 samples.

linear probe	1% (n=7)	5% (n=36)	10% (n=73)	20% (n=146)	100% (n=732)
SimCLR (200k)	0.49 ± 0.02	0.61 ± 0.01	0.66 ± 0.01	0.67 ± 0.02	0.71 ± 0.01
SimCLR-ViT (1M)	0.35 ± 0.03	0.50 ± 0.01	0.55 ± 0.01	0.56 ± 0.01	0.59 ± 0.00
CytoNet (200k)	0.59 ± 0.06	0.72 ± 0.01	0.74 ± 0.00	0.75 ± 0.00	0.77 ± 0.00
CytoNet-ViT (1M)	0.63 ± 0.01	0.73 ± 0.00	0.74 ± 0.00	0.75 ± 0.00	0.77 ± 0.00
finetune					
scratch	0.15 ± 0.10	0.40 ± 0.22	0.65 ± 0.02	0.72 ± 0.02	0.78 ± 0.00
scratch-ViT	0.08 ± 0.05	0.52 ± 0.10	0.65 ± 0.05	0.34 ± 0.41	0.20 ± 0.19
SimCLR (200k)	0.15 ± 0.07	0.45 ± 0.05	0.53 ± 0.07	0.69 ± 0.02	0.76 ± 0.03
SimCLR-ViT (1M)	0.11 ± 0.03	0.38 ± 0.06	0.50 ± 0.14	0.56 ± 0.19	0.45 ± 0.26
CytoNet (200k)	0.23 ± 0.11	0.57 ± 0.02	0.64 ± 0.05	0.73 ± 0.01	0.78 ± 0.02
CytoNet-ViT (1M)	0.05 ± 0.03	0.25 ± 0.18	0.52 ± 0.14	0.78 ± 0.02	0.21 ± 0.33

fixed. Performance for seen brains and the unseen brain was comparable across all choices of transfer brain. Macro-F1 scores for the transfer brain varied somewhat, reflecting differences in the availability and composition of annotated areas across brains. Since macro-F1 is particularly sensitive to missing labels (e.g., a missing label that is incorrectly predicted only once contributes a zero to the average), such variability is expected and does not affect the overall conclusion: our experiments with transfer brain B07 are representative for the proposed approach.

11.5 Visualization of data-driven mapping through clustering

Figure 9 visualizes the annotation-based clustering of areas Fp1 and Fp2 in B06 based on CytoNet-ViT (1M) features. Clusters were manually assigned to represent areas Fp1 or Fp2 based on visual inspection and compared to the reference annotations of the Julich Brain Atlas. The results show a strong alignment between annotations and cluster assignment, with an accuracy of 94.75%.

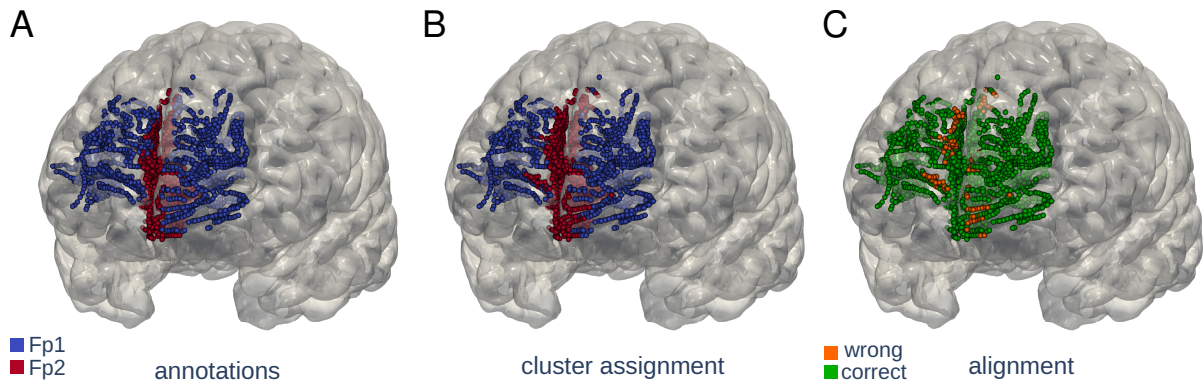


Figure 9: Visualization of annotation-based clustering of areas Fp1 and Fp2 in B06 based on CytoNet-ViT (1M) features. The surface mesh of the Colin 27 reference template is shown for reference. **A:** Points were pre-localized using joint annotations of areas Fp1 and Fp2. **B:** Points were clustered into two clusters using K-means and were assigned to represent areas Fp1 or Fp2 based on visual inspection. **C:** Color-coding of the alignment between annotations and cluster assignment.

11.6 Investigation of shortcut learning in SimCLR

Figure 10 shows a retrieval based analysis for the SimCLR (200k) model for four randomly selected reference image patches.

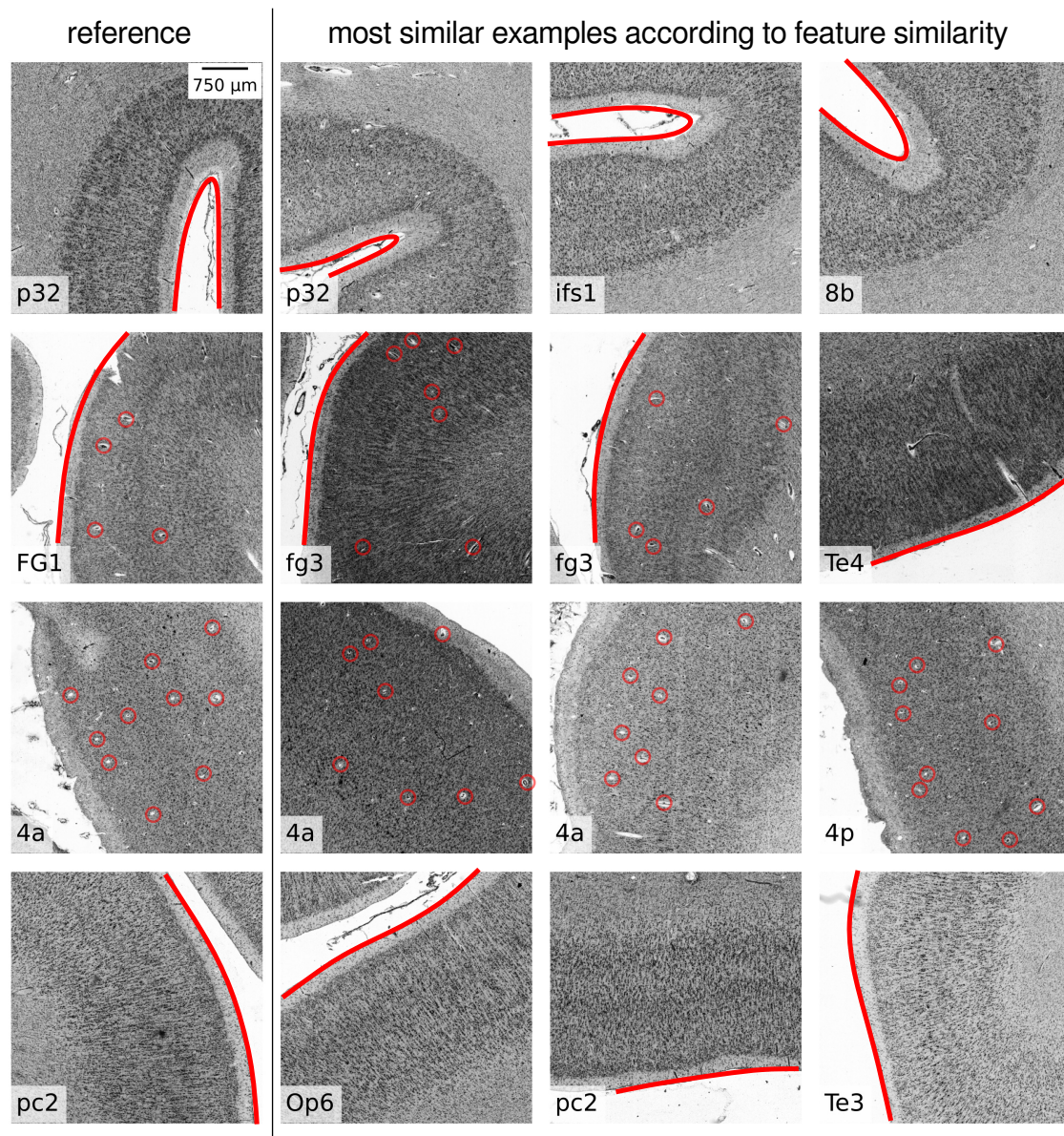


Figure 10: Retrieval-based analysis of features learned by SimCLR (200k), revealing shortcut learning. The left column shows four randomly sampled reference image patches and their corresponding brain area. For each of the selected patches, the three most similar image patches from the dataset are shown, where the similarity is measured by the cosine similarity between their respective SimCLR (200k) features. Image similarity seems to be largely defined by tissue morphology, while being mostly independent of the brain area, and hence, cytoarchitectonic properties. Annotations point out possible confounding factors for the shown examples, including characteristics tissue morphology in rows 1,2,4, or characteristic blood vessel patterns in rows 2 and 3.